A seminar on k-space applied to medical ultrasound

Martin E. Anderson and Gregg E. Trahey

Department of Biomedical Engineering
Duke University

April 12, 2000

Contents

Chapter 1

A brief introduction to ultrasound

Medical ultrasound, also called sonography, is a mode of medical imaging that has a wide array of clinical applications, both as a primary modality and as an adjunct to other diagnostic procedures. The basis of its operation is the transmission of high frequency sound into the body followed by the reception, processing, and parametric display of echoes returning from structures and tissues within the body. Ultrasound is primarily a tomographic modality, meaning that it presents an image that is typically a cross-section of the tissue volume under investigation. It is also a soft-tissue modality, given that current ultrasound methodology does not provide useful images of or through bone or bodies of gas, such as found in the lung and bowel. Its utility in the clinic is in large part due to three characteristics. These are that ultrasound a) is a real-time modality, b) does not utilize ionizing radiation, and c) provides quantitative measurement and imaging of blood flow.

The purpose of this document is to present the ultrasound researcher with methods for characterizing and analyzing ultrasound imaging systems. The central approach is based on linear systems theory, i.e. the use of spatial- and temporal-frequency domain representations of ultrasound system impulse responses and scattering functions to understand and analyze both conventional and hypothetical imaging methods. Spatial frequency domain, or **k-space**, analysis can be a powerful, intuitive tool for the instruction, investigation, and development of ultrasound beamforming techniques[1, 2].

This document is not intended as a general introduction to ultrasound, either in terms of physical acoustics or clinical practice. The authors have included references in the text to some of the many sources of information on these and other related topics that are beyond the scope of this document.

1.1   Resolution, beamforming and the point spread function

A typical transducer uses an array of piezoelectric elements to transmit a sound pulse into the body and to receive the echoes that return from scattering structures within. This array is often referred to as the imaging system's **aperture**. The transmit signals passing to, and the received signals passing from the array elements can be individually delayed in time, hence the term **phased array**. This is done to electronically steer and focus each of a sequence of acoustic pulses through the plane or volume to be imaged in the body. This produces a 2- or 3-D map of the scattered echoes, or **tissue echogenicity** that is presented to the clinician for interpretation. The process of steering and focusing these acoustic pulses is known as **beamforming**. This process is shown schematically in Figure 1.1.
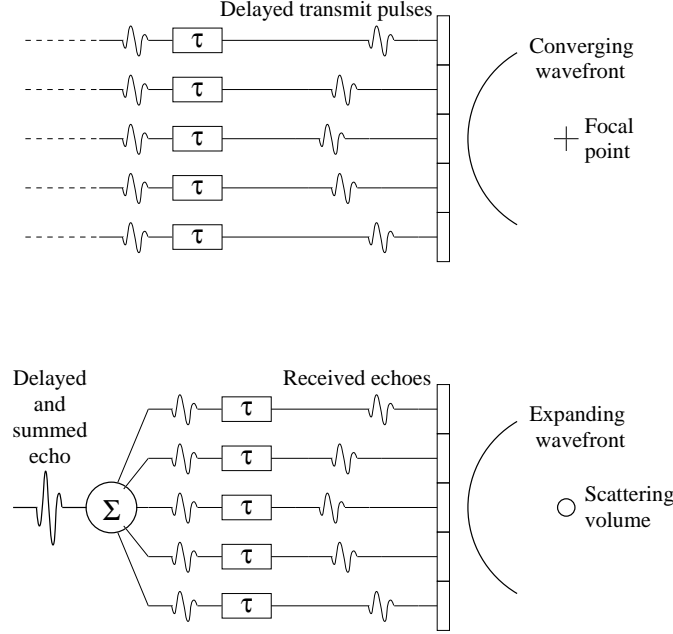
Figure 1.1: A conceptual diagram of phased array beamforming. (Top) Appropriately delayed pulses are transmitted from an array of piezoelectric elements to achieve steering and focusing at the point of interest. (For simplicity, only focusing delays are shown here.) (Bottom) The echoes returning are likewise delayed before they are summed together to form a strong echo signal from the region of interest.

The ability of a particular ultrasound system to discriminate closely spaced scatterers is specified by its spatial resolution, which is typically defined as the minimum scatterer spacing at which this discrimination is possible. The system resolution has three components in Cartesian space, reflecting the spatial extent of the ultrasound pulse at the focus. The coordinates of this space are in the axial, lateral, and elevation dimensions. The axial, or **range**, dimension indicates the predominant direction of sound propagation, extending from the transducer into the body. The axial and the lateral dimension together define the tomographic plane, or slice, of the displayed image. These dimensions relative to the face of a linear array transducer are shown in Figure 1.2. The elevation dimension contains the slice thickness.

A modern ultrasound scanner operating in brightness mode, or **B-mode**, presents the viewer with a gray-scale image that represents a map of echo amplitude, or **brightness,** as a function of position in the region being scanned. In B-mode the ultrasound system interrogates the region of interest with wide bandwidth sound pulses. Such a pulse from a typical array is shown in Figure 1.3.

The acoustic pulse in Figure 1.3 is shown as a function of acoustic pressure over the lateral and axial dimensions. In fact the pulse is a three-dimensional function, with extent in elevation as well. In the terminology of linear systems theory it is the impulse response of the system, and the response of the ultrasound system at the focus is fully characterized by this function. As it represents the output of the ultrasound system during interrogation of an ideal point target, it is also known as the system's **point spread function** (PSF). The character of the PSF in the axial dimension is determined predominantly by the center frequency and bandwidth of the acoustic signal generated at each transducer element, while its character in the lateral and elevation dimensions is determined predominantly by the aperture and element geometries and the beamforming applied. The term
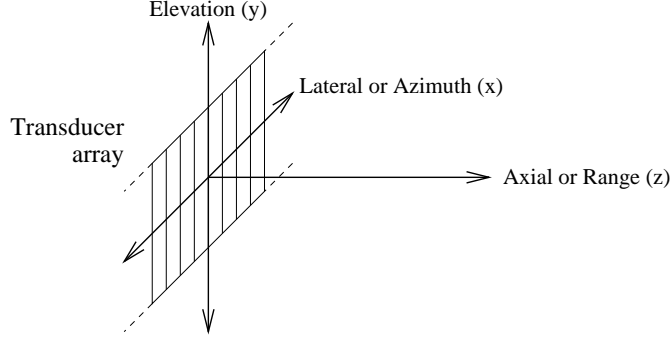
Figure 1.2: A diagram of the spatial coordinate system used to describe the field and resolution of an ultrasound transducer array. Here the transducer is a 1-D array, subdivided into elements in the lateral dimension. The transmitted sound pulse travels out in the axial dimension.

Figure 1.3: The acoustic pulse from a typical array (7.5 MHz, 60% bandwidth, 128 elements of width equal to the wavelength), shown at the acoustic focus. The pulse is displayed as a map of pressure amplitude and is traveling in the positive direction along axial dimension.

PSF is often used to refer to two-dimensional representations of the system response in pressure amplitude versus space, such as that shown in Figure 1.3, with the implicit understanding that the actual response has three-dimensional extent.

In analyzing hypothetical ultrasound systems, predicting the form of the PSF is critical. However, the analytic solution for the PSF for an arbitrary array geometry is usually intractable. Throughout this document, an acoustic field simulation program developed by Jensen and Svendsen was used to predict the acoustic field under the various conditions and array geometries of interest[3]. This program is based on a method developed by Tupholme and Stephanishen[4, 5, 6]. It calculates the convolution of a transmit excitation function, such as a sine wave with Gaussian envelope, with the spatial impulse response of the transducer. The spatial impulse response is the hypothetical pressure pattern created upon excitation of the array with a perfect impulse. The spatial impulse response is not a physically realizable, but serves as a useful calculation tool in this context. This method can accommodate arbitrary geometries by division of the aperture into smaller, rectangular

elements. The spatial impulse response for each element is calculated separately, and then these solutions are combined by superposition to produce that for the entire aperture.

The three components of spatial resolution define a what is called the resolution volume. A modern, high frequency ultrasound transducer has a resolution volume at the focus that is on the order of 300 x 300 x 10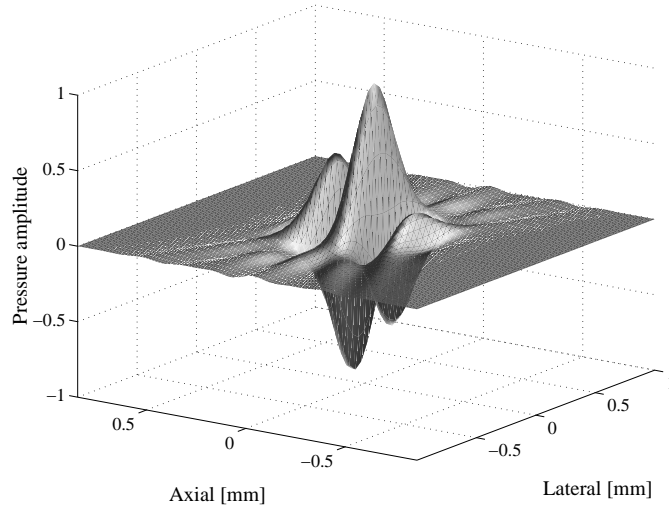00 μm axially, laterally, and in elevation, respectively. The evolution of the dimensions of the acoustic pulse from a typical array (7.5 MHz, 60% bandwidth, 128 elements of width equal to the wavelength, or λ **-pitch**) as it passes through the focal plane with fixed transmit and receive focus is shown in Figure 1.4. This figure plots the -6 dB amplitude contour of the PSF in a sequence of slices. Each slice defines a plane in the lateral-elevational dimensions, and the slices are spaced in the axial dimension. These contours demonstrate how the PSF is most compact at the focus, and also show the resolution mismatch between the lateral and elevation dimensions that is typical of a 1-D array. The axial dimension of the resolution volume is not displayed in this plot.
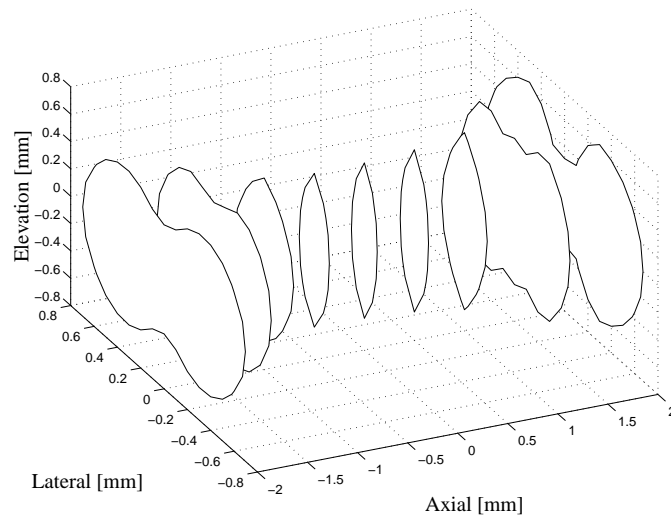
Figure 1.4: This diagram shows how the spatial resolution of the acoustic pulse in the lateral and elevation dimensions changes as it travels in the axial dimension through the focal plane. These acoustic pressure amplitude contours are -6 dB relative to the peak amplitude within each slice of the point-spread function (PSF) as it propagates. Dimensions are relative to the focal point.

The **sound** in ultrasound is a physical longitudinal wave. The compression and rarefaction of the medium at the wavefront causes particle translations on the order of microns. The tissue at the cellular level is perturbed on a bulk level, i.e. the wavelength is much greater than the size of cells.

Here are some numbers of interest to put ultrasound in perspective. At 1 MHz, 100 mW/cm^2 (FDA upper acoustic power limit):

Wavelength	1.5 mm
Phase velocity	1540 m/s = 1.54 mm/μs
Peak particle displacement	0.0057 μm
Peak particle velocity	3.8 cm/sec
Peak particle acceleration	22,452 g
Peak pressure	1.8 atm
Radiation force	0.007 g/cm^2
Heat equivalent	0.024 cal/sec cm^2 (total absorption)

1.2   Sound wave propagation as a linear process

From Insana and Brown, we draw a concise opening paragraph:

> Fluids have elasticity (compressibility κ) and inertia (mass density ρ), the two characteristics required for wave phenomena in a spatially distributed physical system whose elements are coupled. Elasticity implies that any deviation from the equilibrium state of the fluid will tend to be corrected; inertia implies that that the correction will tend to overshoot, producing the need for a correction in the opposite direction and hence allowing for the possibility of propagating phenomena – acoustic pressure waves[7].

Throughout this text we will describe and analyze ultrasound systems in the context of linear acoustics, meaning that pressure wave fields considered are assumed to represent solutions of the the linear wave equation. There are many forms of the wave equation, one of which is

$$\frac{\partial^2 p}{\partial z^2} = \rho_0 \kappa \frac{\partial^2 p}{\partial t^2} \tag{1.1}$$

where p is pressure, ρ_0 is the medium density at equilibrium, and κ is the compressibility. This is a one-dimensional form of the wave equation in time t and position z.

The utility of k-space in ultrasound research grows from the fact that sinusoidal pressure waves both satisfy the multi-dimensional linear wave equation and form the basis set of the multi-dimensional Fourier transform. Thus any system operating under linear conditions has a k-space representation.

In the context of three-dimensional k-space, the general form of the basis function is a continuous plane wave. An example in analytic form would be

$$p(x, y, z, t) = P_0 \cos(2\pi f t + k z) \quad \text{where} \quad k = 2\pi f / c \tag{1.2}$$

for a plane wave of amplitude P_0 and wavenumber k traveling along the z axis in a medium of sound speed c. It is important to note that for this four-dimensional basis function to be represented in 3-D k-space, one of the variables must be held constant (usually time t). We can represent any physically realizable solution of the linear wave equation with a superposition of such plane waves at the appropriate spatial frequencies, amplitudes, and phases.

1.3   The scattering and reflection of sound

Medical ultrasound imaging relies utterly on the fact that biological tissues scatter or reflect incident sound. Although the phenomenon are closely related, in this text **scattering** refers to the interaction between sound waves and particles that are much smaller than the sound's wavelength λ, while **reflection** refers to such interaction with particles or objects larger than λ.

The scattering or reflection of acoustic waves arise from inhomogeneities in the medium's density and/or compressibility. Sound is primarily scattered or reflected by a discontinuity in the medium's mechanical properties, to a degree proportional to the discontinuity. (By contrast, continuous changes in a medium's material properties cause the direction of propagation to change gradually.)

The elasticity and density of a material are related to its sound speed, and thus sound is scattered or reflected most strongly by significant discontinuities in the density and/or sound speed of the medium. A thorough review of the mechanisms of scattering is provided by Insana and Brown[7].

1.3.1 Scatterer sizes less than and equal to the wavelength

Consider a medium subjected to acoustic insonification, and a particle in this medium that is much smaller than the wavelength of the sound. If this particle is of the same density and compressibility as the medium, it scatters no sound at all. If its density is the same but its compressibility is different, it will react to the surrounding pressure variation by radially expanding and contracting differently than the surrounding medium. This type of scatterer gives off **monopole radiation**, shown in Figure 1.5. If these conditions are reversed, i.e. the particle's compressibility is the same as the surrounding medium but its density is different, the particle's motion in response to the incident wave will not equal that of the medium, and it will move back and forth in relation to the medium. This type of scattering gives off **dipole radiation**, also shown in Figure 1.5. Most real sub-wavelength scatterers emit some combination of monopole and dipole radiation, although one may dominate significantly over the other.
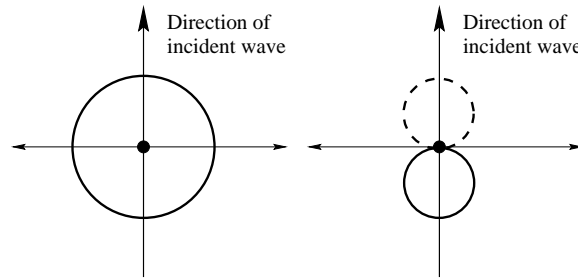

Figure 1.5: (Left) The pressure amplitude pattern of monopole radiation from a "compressibility" scatterer is isotropic. (Right) The corresponding pattern of a "density" scatterer is highly directional, corresponding to two closely-spaced monopoles operating out of phase. The pattern exhibits a 180° phase shift along the axis of sound propagation, and a null surrounding the scatterer and normal to this axis.

The radiation pattern becomes more complex as the scatterer size approaches the wavelength of the incident sound. The analytic solution for the radiation pattern from a spherical elastic scatterer in a fluid was first described by Faran[8]. The radiation pattern of such a scatterer is dependent on the material properties of the sphere and the medium and on the sphere's radius. Also, the result depends on whether one includes the effects of sound penetrating into the sphere and reverberating, which distinguishes the "elastic" from the "inelastic" solution. Faran solutions for radiation magnitude vs. scattering angle are shown in Figures 1.6 and 1.7 for a range of sphere radii, parameterized by the sphere radius a and the wavenumber of insonification $k = 2\pi/\lambda$, and using the material properties of crown glass ($c = 5100$ m/s, $\rho = 2.4$ gm/cm^3, $\sigma = 0.24$) in 20° water[9]. Faran defines the scattering angle such that the sound source is at 180°. These figures show that as the scatterer radius is increased up to and beyond the wavelength of the sound, the radiation pattern becomes progressively more *directional*.

We can make several other observations using the Faran model. In Figure 1.8 we consider the magnitude of the sphere's echo back at the source as a function of ka, the product of the frequency and the sphere's radius. In the left half of the figure, we consider $ka < 1$, and observe that
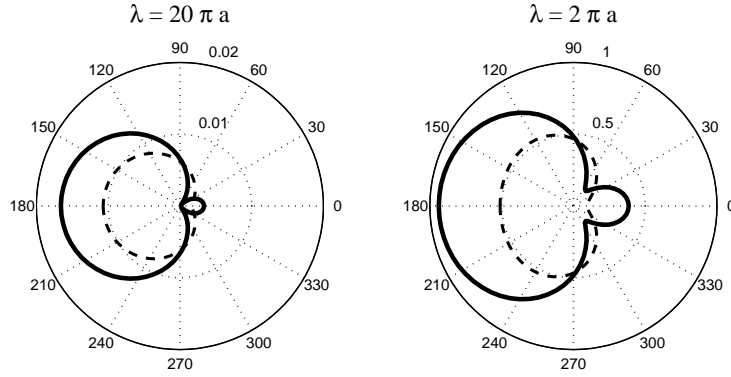
Figure 1.6: Angular scattering from elastic (solid) and inelastic (dashed) spheres of circumference $\leq \lambda$. The insonification source is located at $180°$.
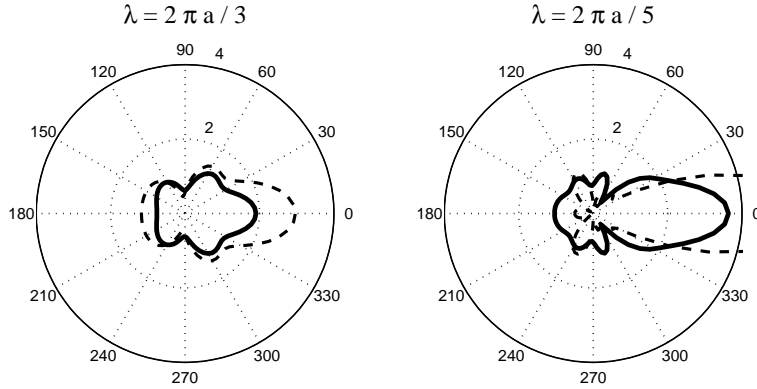

Figure 1.7: Angular scattering from elastic (solid) and inelastic (dashed) spheres of circumference $> \lambda$. The insonification source is located at $180°$.

the echo magnitude for this condition (solid line) is roughly comparable to $(ka)^2$ (dashed line). In other words, the echo magnitude of scatterers significantly smaller than the wavelength has an f^2 dependence. When echo magnitude $|A|$ is converted to intensity $|A|^2$, this dependence is approximately f^4. Scatterers that are much smaller than the wavelength are known as **Rayleigh scatterers**, and are generally considered to have an f^4 intensity dependence.

Also shown in Figure 1.8 is a graph of the backscatter echo magnitude (i.e. scattering angle = $180°$) for $0 < ka < 10$. As before, the material properties used in the model are those for crown glass. The elastic (solid) and the the inelastic (dashed) solutions are contrasted. For a fixed diameter a, this Faran solution corresponds to a scatterer "frequency response". It is seen that when the solution includes the effects of sound penetrating into the sphere and reverberation within the sphere, this spectrum develops complex nulls and peaks. Thus reverberation of sound within a scatterer results in a echo response that can be highly frequency dependent, and markedly different from the response predicted *without* accounting for these effects. One the other hand, the inelastic response is adequate for materials with density and/or sound speed *much* greater than those of the surrounding fluid. Comprehensive tables of the acoustic parameters of materials and of biological tissues can be found in [9], [10], and [11].
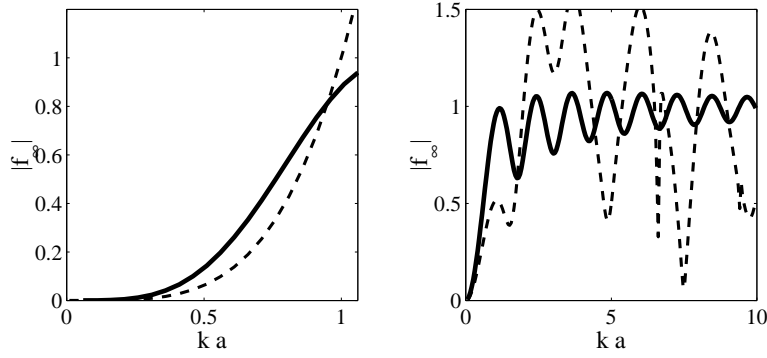
Figure 1.8: (Left) The backscatter amplitude for a sphere for $ka < 1$ (solid) is compared to $(ka)^2$ (dashed), showing that for scatterers smaller than the wavelength, echo amplitude as a f^2 dependence, corresponding to an intensity dependence of f^4, a characteristic of Rayleigh scattering. (Right) The backscatter amplitude for a sphere as a function of frequency is compared for the elastic (dashed) and inelastic (solid) cases, showing how internal reverberation of sound within a scatterer can create peaks and nulls in the scattering spectrum.

1.3.2   Reflecting structures larger than the wavelength

Tissue structures within the body feature boundaries on a scale much larger than the wavelength. Prominent **specular** echoes arise from these boundaries. The acoustic properties of tissues are often characterized using the concept of **acoustic impedance** Z. $Z = \rho_0 c = \sqrt{\rho_0 c_{elas}}$, where ρ_0 is the density of the tissue, c is the sound speed, and c_{elas} is the tissue elasticity. When a wave is directly incident on a boundary between two media with acoustic impedances Z_1 and Z_2, the ratio of incident to reflected pressure is predicted by the reflection coefficient R, defined as:

$$R = \frac{Z_2 - Z_1}{Z_2 + Z_1} \tag{1.3}$$

It is important to note that in ultrasound, as in optics, tissue boundaries can also give rise to refraction that can produce image artifacts, steering errors, and aberration of the beam. A more general form of Equation 1.3 describes reflection and refraction as a function of incident angle, where the incident and transmitted angles θ_i and θ_t, shown in Figure 1.9, are related by Snell's Law:

$$R = \frac{(Z_2/\cos\theta_t) - (Z_1/\cos\theta_i)}{(Z_2/\cos\theta_t) + (Z_1/\cos\theta_i)} \quad \text{where} \quad \frac{\sin\theta_i}{\sin\theta_t} = \frac{\lambda_1}{\lambda_2} = \frac{c_1}{c_2} \tag{1.4}$$

It is obvious that ultrasound imaging relies on reflected sound to create images of tissue boundaries and structures. A more subtle fact is that it relies on the transmitted component of the wave as well. If all the transmitted sound energy is reflected at a particular interface due to a particularly severe acoustic impedance mismatch, no sound penetrates further to illuminate underlying structures. A good example of such a mismatch in the body is the boundary between tissue and air, such as in the lungs. This accounts for the inability of ultrasound to image tissues within or lying under the lung.
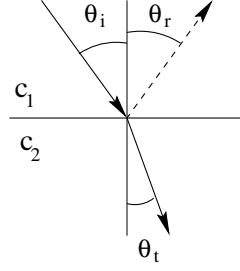
Figure 1.9: The geometry of reflection and refraction at a boundary between media with different sound speeds (see text).

1.3.3 Coherent and incoherent scattering

In this section we have discussed scattering by individual scatterers and reflection by specular targets. A more typical type of scattering in the bodies arises from a diffuse population of sub-resolution scatterers. If the arrangement of these scatterers is spatially random, the resulting **incoherent** scattering gives rise to **speckle noise**. If the scatterers have a periodic arrangement, a **coherent** component is introduced, producing periodicity in the echo spectrum. Both incoherent and coherent scattering will be discussed further in following sections.

Chapter 2

Ultrasound and Fourier optics

2.1 Propagation as a linear operation

As discussed in Section 1.2, linear propagation is governed by the linear wave equation. An important consequence of representing propagation of sound as a linear process is that we can apply the superposition principle.

The **Huygen-Fresnel principle** states that wavefronts can be decomposed into a collection of point sources, each the origin of a spherical, expanding, wave that can be represented as a free space Green's function. This concept underlies the derivation of an important tool, the Fraunhofer Approximation.

2.2 The significance of the Fraunhofer approximation

The **Fraunhofer approximation** (FA) plays a pivotal role in our exploration of ultrasound k-space. In a nutshell, this well-known expression from the optics literature states that the far-field complex amplitude pattern produced by a complex aperture amplitude function is approximately equal to 2-D Fourier transform of that function. Applied to ultrasound, this approximation states that the ultrasound beam's pressure amplitude pattern can be estimated by taking the 2-D Fourier transform of the transducer aperture. Naturally, this approximation is based on several assumptions and requirements that constrain its application to the far field of an unfocused transducer or the focal plane of a focused transducer. While the approximation is based on a single frequency, or **monochromatic** solution, we can extend its application to broadband cases through superposition. As we shall see, the pattern is parameterized by the frequency of the wave emitted at the aperture.

As long as we don't violate the assumptions made in formulating the FA, this powerful approximation allows us to extend our intuition regarding linear systems to the study of ultrasound beamforming. Restricting the discussion for a moment to the lateral and axial dimensions, the most obvious example of an aperture function is the rectangular aperture of a linear array lying along the lateral coordinate axis, emitting a single frequency of sound. Representing this aperture function as a **rect** and applying the FA, we can guess that the ultrasound pressure amplitude pattern in the far field of this aperture is a **sinc** function.

2.3 The development of the Fraunhofer approximation

The complete theoretical development of the FA, from which these excerpts are drawn, can be found in Goodman's *Introduction to Fourier Optics*[12]. The coordinate system used is this discussion
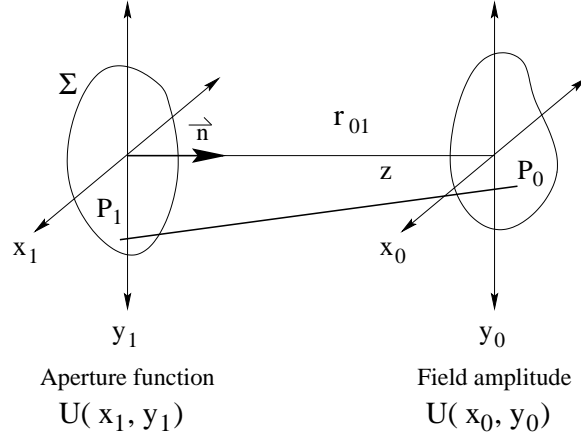

Figure 2.1: Coordinate system used in the derivation of the Fraunhofer approximation.

is shown schematically in Figure 2.1. We consider an arbitrary aperture Σ in the aperture plane (x_1, y_1) emitting monochromatic radiation of wavenumber k, spatially weighted with a complex amplitude function $U(x_1, y_1)$. The object is to determine the complex field pattern at an observation plane $U(x_0, y_0)$. The geometric path length between any two points P_0 and P_1 is simply:

$$r_{01} = \sqrt{z^2 + (x_1 - x_0)^2 + (y_1 - y_0)^2} \tag{2.1}$$

Consider the application of Huygen's principle to the aperture, i.e. that this arbitrary, spatially extended source is represented by an infinite number of point sources lying across Σ, each with a particular amplitude and phase defined by $U(x_1, y_1)$. The amplitude $U(P_0)$ observed at point P_0 can be determined by adding up the contributions of all of these point sources after taking into account the geometric path lengths from all of these sources to P_0. This concept is mathematically expressed in a Huygen-Fresnel integral:

$$U(P_0) = \iint_\Sigma h(P_0, P_1) U(P_1) ds$$

$$\text{where } h(P_0, P_1) = \frac{1}{j\lambda} \frac{\exp(jkr_{01})}{r_{01}} \cos(\overrightarrow{n}, \overrightarrow{r}_{01}) \tag{2.2}$$

The function $h(P_0, P_1)$ combines a Green's function $\exp(jkr_{01})/r_{01}$ representing a spherically expanding wave with what is known as an **obliquity term,** $\cos(\overrightarrow{n}, \overrightarrow{r}_{01})$ (the cosine of the angle between $\overrightarrow{n}$ and $\overrightarrow{r}_{01}$). This Huygen-Fresnel integral sums the contributions from an infinite number of sources across the aperture surface Σ. One can also think of the propagation of waves from these sources over the distance between $U(x_1, y_1)$ and $U(x_0, y_0)$ as a kind of filter that has an impulse response $h(P_0, P_1)$.

13

Elaborating on Eq. 2.2:

$$U(x_0, y_0) = \iint_\Sigma h(x_0, y_0; x_1, y_1) U(x_1, y_1) dx_1 dy_1$$

$$U(x_0, y_0) = \iint_{-\infty}^{\infty} h(x_0, y_0; x_1, y_1) U(x_1, y_1) dx_1 dy_1,$$

with $U(x_1, y_1) = 0$ outside the aperture Σ

(2.3)

We now introduce the first assumption, known as the **small angle approximation**:

$$cos(\overrightarrow{n}, \overrightarrow{r}_{01}) \approx 1$$

$$r_{01} \approx z$$

$$h(x_0, y_0; x_1, y_1) \approx \frac{1}{j\lambda z} \exp(jkr_{01})$$

(2.4)

2.3.1 The Fresnel approximation

This is an intermediate step on the way to the Fraunhofer approximation. Given the expression for path length,

$$r_{01} = \sqrt{z^2 + (x_1 - x_0)^2 + (y_1 - y_0)^2}$$

$$= z\sqrt{1 + \left(\frac{(x_1 - x_0)}{z}\right)^2 + \left(\frac{(y_1 - y_0)^2}{z}\right)}$$

(2.5)

we introduce a truncated binomial expansion:

$$\sqrt{1 + b} = 1 + \frac{1}{2}b - \frac{1}{8}b^2 + \dots$$

used to approximate r_{01} truncated to 2 terms:

$$r_{01} \approx z\left[1 + \frac{1}{2}\left(\frac{(x_1 - x_0)}{z}\right)^2 + \frac{1}{2}\left(\frac{(y_1 - y_0)}{z}\right)^2\right]$$

(2.6)

Therefore:

$$h(x_0, y_0; x_1, y_1) \approx \frac{\exp(jkz)}{j\lambda z} \exp\left[\frac{jk}{2z}\left[(x_1 - x_0)^2 + (y_1 - y_0)^2\right]\right]$$

(2.7)

2.3.2 The Fraunhofer approximation

After rearranging terms:

$$h(x_0, y_0; x_1, y_1) \approx \frac{\exp(jkz)}{j\lambda z} \exp\left[\frac{jk}{2z}\left[(x_0^2 + y_0^2)\right]\right]$$

$$\times \exp\left[\frac{jk}{2z}\left[(x_1^2 + y_1^2)\right]\right] \exp\left[-\frac{jk}{z}\left[(x_0 x_1 + y_0 y_1)\right]\right]$$

(2.8)

The Fraunhofer assumption is that the distance between the aperture plane and the observation plane is much greater than the dimensions of the aperture function, i.e.:

$$z >> \frac{k(x_1^2 + y_1^2)_{\text{max}}}{2} \tag{2.9}$$

The distance at which this approximation becomes reasonable is known as the **Fraunhofer distance**. Thus this quadratic phase term in Eq. 2.8 is assumed to be ≈ 1. Finally:

$$U(x_0, y_0) \approx \frac{\exp(jkz) \exp\left[\frac{jk}{2z}(x_0^2 + y_0^2)\right]}{j\lambda z} \iint_{-\infty}^{\infty} U(x_1, y_1) \exp\left[-\frac{j2\pi}{\lambda z}(x_0 x_1 + y_0 y_1)\right] dx_1 dy_1 \tag{2.10}$$

Aside from the quadratic phase term outside the integral, this result is the Fourier transform of $U(x_1, y_1)$ evaluated at spatial frequencies

$$f_x = \frac{x_0}{\lambda z} \quad \text{and} \quad f_y = \frac{y_0}{\lambda z}. \tag{2.11}$$

2.4   The two-dimensional Fourier transform

The Fraunhofer approximation is a powerful tool for understanding ultrasound beamforming. Its intuitive application requires knowledge of 2-D Fourier Fourier transforms and transform properties. These are seen to be extensions of the Fourier transforms and properties in 1-D, with the addition of the issue of **separability**.

2.4.1   The analytic form of the 2-D Fourier transform

Following Bracewell's *The Fourier Transform and Its Applications*[13], the relationships between a 2-D function $f(x, y)$ and its 2-D Fourier transform are:

$$\begin{aligned} F(u, v) &= \iint_{-\infty}^{\infty} f(x, y) \, exp\big(-j2\pi(ux + vy)\big) \, dx \, dy \\ f(x, y) &= \iint_{-\infty}^{\infty} F(u, v) \, exp\big(j2\pi(ux + vy)\big) \, du \, dv \end{aligned} \tag{2.12}$$

The convolution integral is another extension to 2-D of a familiar relationship:

$$f(x, y) * g(x, y) = \iint_{-\infty}^{\infty} f(\eta, \nu) \, g(x - \eta, y - \nu) \, d\eta \, d\nu \tag{2.13}$$

A 2-D function is **separable** if it can be described as the product of two 1-D functions along orthogonal dimensions:

$$\begin{aligned} f(x, y) &= f(x)f(y) \\ F(u, v) &= F(u)F(v) \end{aligned} \tag{2.14}$$

Thus if a function is separable in the space domain, it is also separable in the frequency domain, and vice versa. Identifying a function as separable can simplify its analysis by reducing its 2-D transform to a product of 1-D transforms. Identifying a function as separable can simplify its analysis by reducing its 2-D transform to a product of 1-D transforms.

One class of functions that are **not** separable are those having **circular symmetry**. The 2-D Fourier transforms of these functions are also circularly symmetric:

$$\text{If } f(x,y) = f(r), \text{ where } r^2 = x^2 + y^2$$
$$\text{then } F(u,v) = F(q), \text{ where } q^2 = u^2 + v^2 \tag{2.15}$$

A series of Fourier transform pairs are shown in Figures 2.2 through 2.10 using Bracewell's notation for the delta (δ), comb (III), rectangle (Π), and triangle (Λ) functions.
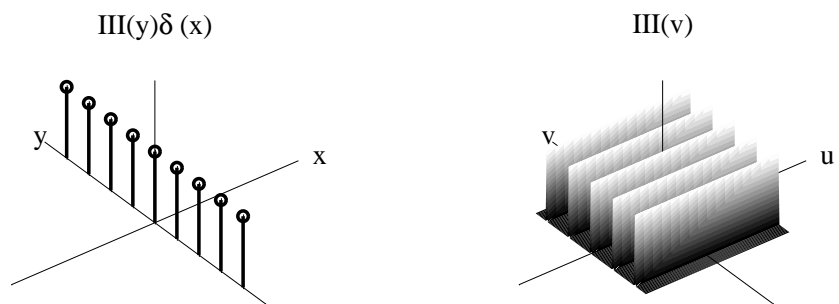
III(y)δ (x)

III(v)

Figure 2.2:

δ (x)

δ (u)

Figure 2.3:

^{2}δ(x,y)

A(u,v)

Figure 2.4:

17

$$\cos 2\pi x$$

$$1/2 \; {}^2\delta \, (u{-}1,v) + 1/2 \; {}^2\delta \, (u{+}1,v)$$

Figure 2.5:

$$\cos \, [2\pi(x \cos \theta + y \sin \theta)]$$

$$1/2 \; {}^2\delta \, [(u{-}1)\cos\theta,(v{-}1)\sin\theta] \; +$$
$$1/2 \; {}^2\delta \, [(u{+}1)\cos\theta,(v{+}1)\sin\theta]$$

Figure 2.6:

$$\cos(2\pi x) \cos(2\pi y)$$

$$1/2 \; {}^2\delta \, (u{-}1,v) + 1/2 \; {}^2\delta \, (u{+}1,v) \; *$$
$$1/2 \; {}^2\delta \, (u,v{-}1) + 1/2 \; {}^2\delta \, (u,v{+}1)$$

Figure 2.7:

18

$\exp[-\pi\,(x^2 + y^2)]$

$\exp[-\pi\,(u^2 + v^2)]$

Figure 2.8:

$\Pi(x)\Pi(y)$

$\text{sinc}(u)\,\text{sinc}(v)$

Figure 2.9:

$\Lambda(x)\Lambda(y)$

$\text{sinc}^2(u)\,\text{sinc}^2(v)$
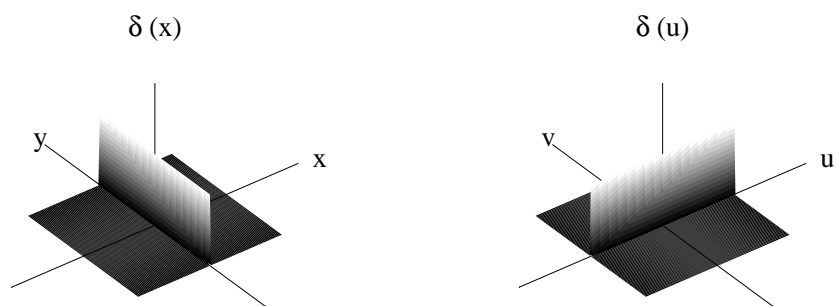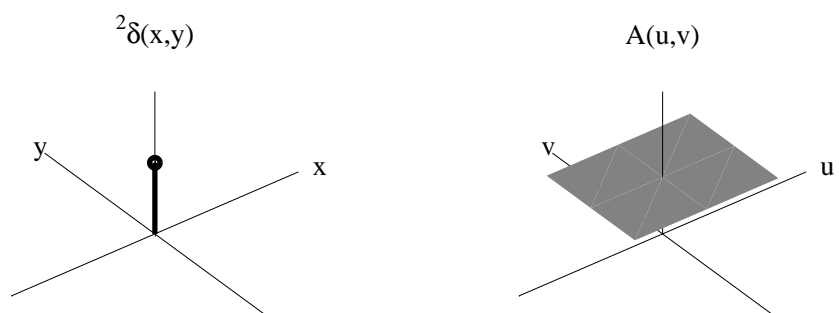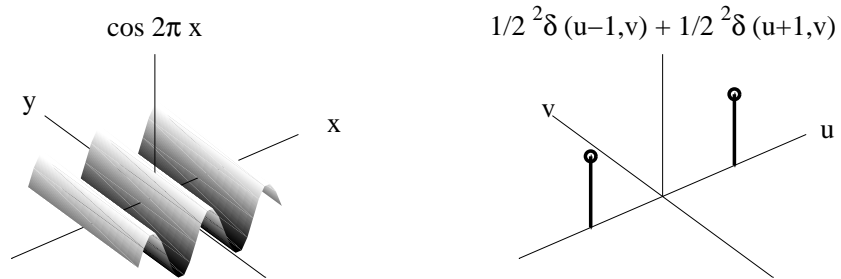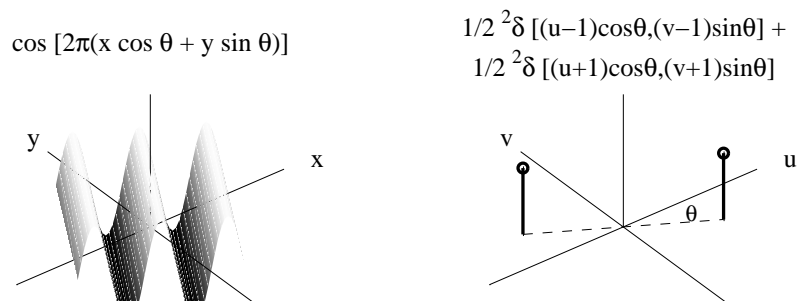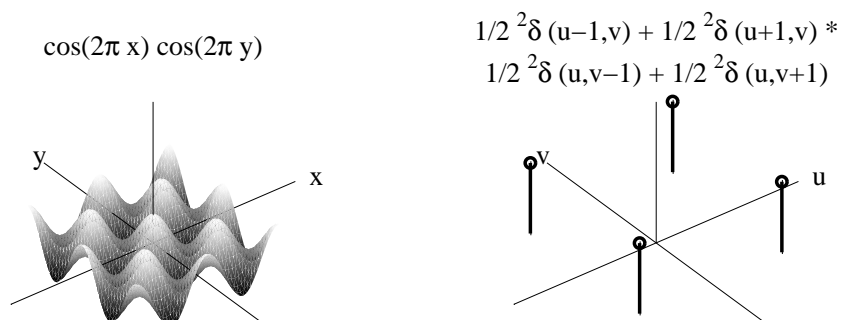
Figure 2.10:

2.4.2   Important properties of the 2-D Fourier transform

$$\text{Scaling: } f(ax, by) \iff \frac{1}{|ab|} F\left(\frac{u}{a}, \frac{b}{b}\right)$$

$$\text{Addition: } f(x,y) + g(x,y) \iff F(u,v) + G(u,v)$$

$$\text{Translation / shift: } f(x-a, y-b) \iff exp\big(-2\pi j(au + bv)\big) F(u,v)$$

(2.16)

$$\text{Convolution: } f(x,y) * g(x,y) \iff F(u,v)\ G(u,v)$$
$$\text{Autocorrelation: } f(x,y) * f^*(-x,-y) \iff |F(u,v)^2|$$
$$\text{Cross-correlation: } f(x,y) * g^*(-x,-y) \iff F(u,v)\ G^*(u,v)$$

$$\text{Power: } \int_{-\infty}^{\infty} f(x,y) g^*(x,y)\ dx\ dy = \int_{-\infty}^{\infty} F(u,v)\ G^*(u,v)\ du\ dv$$

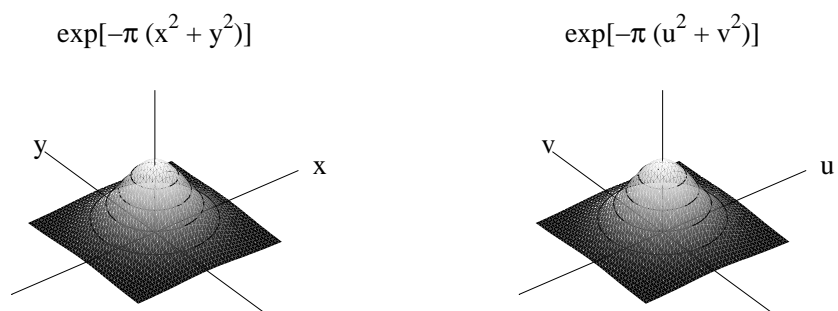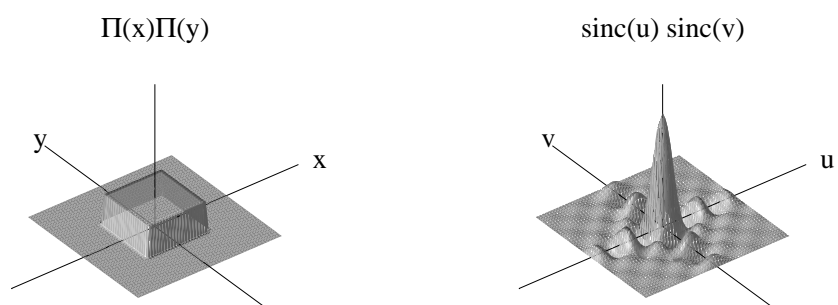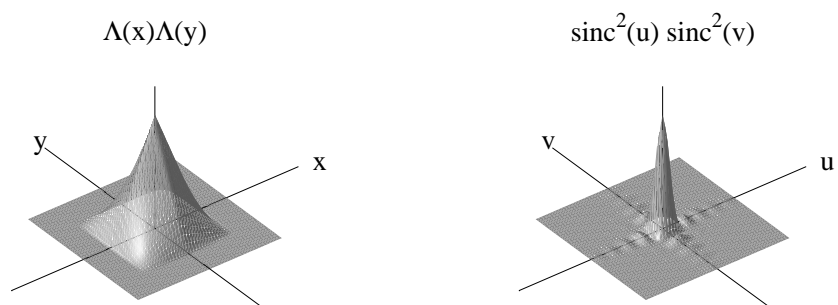### 2.4.3   Transforms and properties in the context of a typical aperture

The basis set of the Fourier transform is the complex exponential of general form $A \exp(j2\pi fx + \theta)$. In systems with circular symmetry, such as most optical systems constructed with circular lenses, a different basis set and transform are usually applied, i.e. Bessel functions and the Hankel transform. These allow a circularly symmetric 2-D problem to be solved as a 1-D function of radius r. In ultrasound, functions with this symmetry are encountered in work with circular pistons. In this text, we restrict our application of the Fraunhofer approximation to the Fourier transform.

The aperture of a typical 1-D linear array ultrasound transducer is rectangular with electronic focusing applied along the longer dimension (lateral) and an acoustic lens providing a fixed focus in the second dimension (elevation). With no **apodization** (amplitude weighting of the elements) this aperture function can be represented as a separable product of two rectangle functions, $\Pi(x)\Pi(y)$. As seen in Figure 2.9, the far-field amplitude pattern of this aperture on transmit or receive is approximated by $\text{sinc}(u)\text{sinc}(v)$.

When this aperture is used on *both* transmit and receive, as is almost always the case, the corresponding function is $\text{sinc}^2(u)\text{sinc}^2(v)$, seen in Figure 2.10. In both cases, the far-field pattern is approximated by these Fourier transforms evaluated at spatial frequencies $f_u = \lambda z/x_o$ and $f_v = \lambda z/y_o$. Intuitively, the transmit beam pattern shows where sound is sent *into* the field, while the receive beam pattern shows the spatial *sensitivity* of the transducer to returning echoes.

To achieve electronic focusing, one or more dimensions of an aperture is typically divided into discrete elements that are themselves small rectangles. The subdivided dimension is more accurately modeled as a small rectangle convolved with a comb function the length of the array. Thus an aperture of size D composed of elements of size d is modeled as $\Pi(D)\ [\Pi(d) * \text{III}(x/d)]$, where $\text{III}(x) = \Sigma_{-\infty}^{\infty} \delta(x-n)$. The transform of this function is a narrow sinc function convolved with a comb, all multiplied by a broad sinc function:

$$\Pi(D)\ [\Pi(d) * \text{III}(x/d)] \iff \text{sinc}(u/d)\ [\text{sinc}(u/D) * \text{III}(du)] \tag{2.17}$$

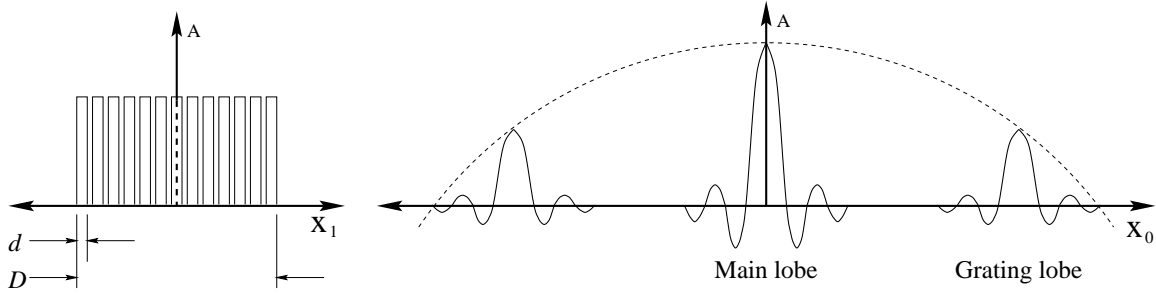This is shown schematically in Figure 2.11.

Figure 2.11: (Left) An aperture of size D composed of elements of size d is modeled as $\Pi(D)$ $[\Pi(d) *$ $\text{III}(x/d)]$. The Fourier transform of this pattern (right) is $\text{sinc}(u/d)$ $[\text{sinc}(u/D) * \text{III}(du)]$. The subdivision of the array into elements produces grating lobes.

The transforms of the individual element and of the entire array have a number of implications. First, each individual element has its own far-field amplitude pattern. This pattern in part determines the angular sensitivity of the element, and by extension, of the entire array. This shows up as the broad sinc pattern in Figure 2.11. Also, the periodicity created by subdividing the array introduces a periodicity in the beam pattern. The desired **main lobe** of the beam pattern is now duplicated off axis as a series of **grating lobes**. These can be a source of image artifacts, as they literally correspond to regions of unintended off-axis emission and sensitivity. The magnitude of these grating lobes is an important design parameter. When the element spacing, or **pitch**, is reduced to λ, the side lobes are located at $90°$ off the main lobe. With a pitch of $\lambda/2$, the grating lobes are practically eliminated. This approach is necessary when the beam is to be aggressively steered off axis, such as in a cardiac probe. The array's angular sensitivity and the distance of the grating lobes off-axis are both dependent on the element size, so it is common to increase the element size beyond $\lambda/2$ and rely on the reduced angular sensitivity of the elements to reduce the impact of the grating lobes. This design approach is appropriate for linear arrays that will not be used with aggressive beam steering.

2.5 Propagation as a spatial transfer function

Under most circumstances in medical imaging, propagation is a linear operation. It has a transfer function associated with it, which is in turn the Fourier transform of the impulse response. (Recently non-linear imaging has also been introduced in clinical scanners, but this modality is beyond the scope of this discussion.)

The free-space Green's function is an impulse function. We can use it to represent a point source, and therefore its Fourier transform is the transfer function of propagation, $H(f_x, F_y) = \exp(jkz)\exp(-j\pi\lambda z(f_x^2 + f_y^2))$. Note that only a change in phase occurs in this operation. There is no change in amplitude, i.e. a pattern at the Fraunhofer distance is the Fourier transform of the aperture, and its Fourier transform gives the aperture distribution back again.

Remember that for an unfocused transducer the FA is only valid beyond the Fraunhofer distance, $z >> k(x_1^2 + y_1^2)_{max}$, such that the greatest off-axis point in the aperture function satisfies the small angle approximation. For a focused transducer, the FA is valid in the focal plane. This is because at the focal point, the spherically converging waves emanating from the focused aperture are indistinguishable from plane waves modulated by a much more distant, unfocused aperture.

Focusing brings the far-field pattern to the focal plane.

To summarize, k-space analysis is based on representing an optical or ultrasound system as a linear system in complex amplitude. Propagation itself can be represented as a transfer function. Under the conditions of linear propagation, only the phase and amplitude of frequency components are modified.

Chapter 3

Ultrasound and k-space

3.1 K-space transforms of elementary geometries

Consider the simple geometry of two sound point sources and an observation plane, shown in Figure 3.1. This corresponds to an impulse pair aperture function, and the FA predicts that we will observe a sinusoidal far-field pattern. This pattern can also be constructed by geometrically predicting the locations of constructive and destructive interference between waves from the two sources. The
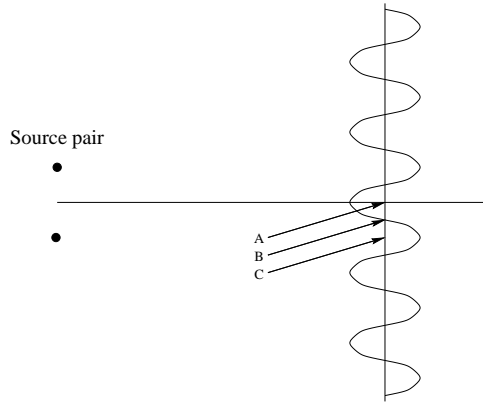

Figure 3.1: Consider the field produced by a pair of sound sources generating constant 1 MHz signals in phase. If we moved a hydrophone across the field it would measure a 1 MHz signal modulated in amplitude and shifted in phase. Locations of constructive interference, such as A and C, alternate with locations of destructive interference, such as B.

Fourier transform of the aperture gives the lateral modulation of the point spread function. The Fourier transform of this point spread function gives the transmit-only or receive-only transfer function of the system in k-space. The system response is equal to the product of the receive-only and the transmit-only responses:

$TxRx(\theta) = Rx(\theta) \times Tx(\theta)$

We refer to the transmit-receive response $TxRx(\theta)$ as the **pulse-echo** response. For the two-source geometry shown in Figure 3.1, the pulse-echo response is contrasted with the transmit-only response in Figure 3.2. The corresponding k-space representations are shown in Figure 3.3.
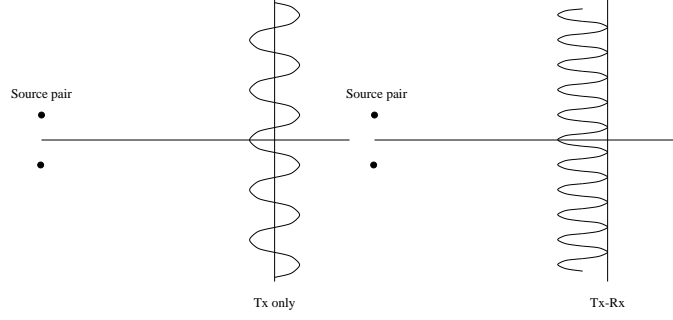
Figure 3.2: The transmit-only (left) and transmit-receive (right) amplitude in the observation plane of a two-element system.
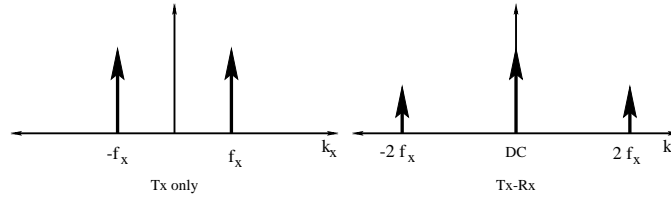

Figure 3.3: The transmit-only (left) and transmit-receive (right) lateral k-space responses of a two-element system.

These solutions for a simple two-source geometry have been for the monochromatic case, i.e. for constant insonification with a single frequency. In these cases the far-field interference pattern in the observation plane technically stretches to infinity. If we consider a broadband case in which each source launches a short pulse, interference occurs only over a limited region in the observation plane, as shown in Figure 3.4. Outside of this region, the path length difference between the two sources and the observation point exceeds the pulse length, and hence interference no longer takes place.

As shown in Figure 3.5, a two-element system with two-frequency output is sensitive to six spatial frequencies, with the redundant frequencies having twice the amplitude of the outliers. As the target gets further away, the outlying spatial frequencies move in as the point spread function spreads out.

3.2   Spatial resolution and spatial frequencies

The relationship between spatial resolution and spatial frequency response can be illustrated with an example based on a rudimentary imaging system. Consider the imaging of two point targets with a single point transducer, as shown in Figure 3.6. This transducer has no lateral resolution whatsoever, and is capable only of resolving targets in range. Another way of stating this is that this imaging system is not sensitive to lateral spatial frequencies. When the point target are equidistant, i.e. only separated in the lateral dimension, it is clear that their echoes cannot be resolved by the point transducer. When the transducer is moved through an arc, the lateral and axial spatial frequencies of the original transducer/target geometry are gradually exchanged. When the transducer has been rotated 90° about the targets, the targets can be resolved provided they are separated by more than the axial resolution of the transducer (i.e. approximately half the pulse
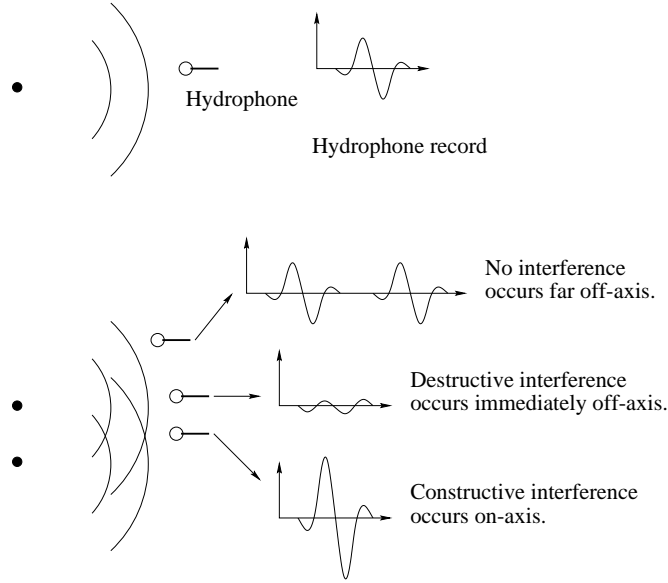
Figure 3.4: Hydrophone responses to pulses emitted by single-source (top) and double-source (bottom) systems. Neglecting diffractive effects, in the single-source system the pulse shape is relatively constant across the field. In the double-source system, interference occurs at points in the field where the pulses overlap. Beamforming is in essence the manipulation of this interference.

length). It is instructive to consider this example in k-space using the rotation property of the 2-D Fourier transform.

By extension, this example demonstrates why an aperture with some lateral extent is required to provide lateral resolution (i.e. lateral extent provides sensitivity to lateral spatial frequencies), and that given a finite target range and a very short pulse, the lateral resolution will only equal the axial resolution if the aperture becomes infinitely large.

3.3 K-space transforms of large apertures and arrays

The idealized k-space examples presented so far consider monochromatic imaging systems with point sources and receivers. Practical imaging systems utilize elements of some finite lateral extent in the aperture, producing pulses with some bandwidth. The k-space response of such a system has some extent, i.e. it forms a "*cloud*" rather than being composed of delta functions. As the number of array elements is increased, this response covers a larger region of support, as seen in Figure 3.7. A sparse array creates gaps in the k-space response. The lateral response and can be predicted by the convolution of the transmit and receive aperture functions, as shown in Figure 3.8.

With a large aperture and negligible kerf, the k-space magnitude response becomes smooth and continuous over a finite region. For a rectangular aperture producing a pulse with a Gaussian frequency response, this k-space frequency response is shaped like an asymmetrical mountain, with a tear-drop shaped footprint.

The lateral pulse-echo transfer function for a rectangular aperture is a triangle. The lateral k-space response is a sinc^2 function. For a broadband transducer, the axial response is often approximated as a Gaussian centered at the transducer's center frequency. These responses are shown in Figure
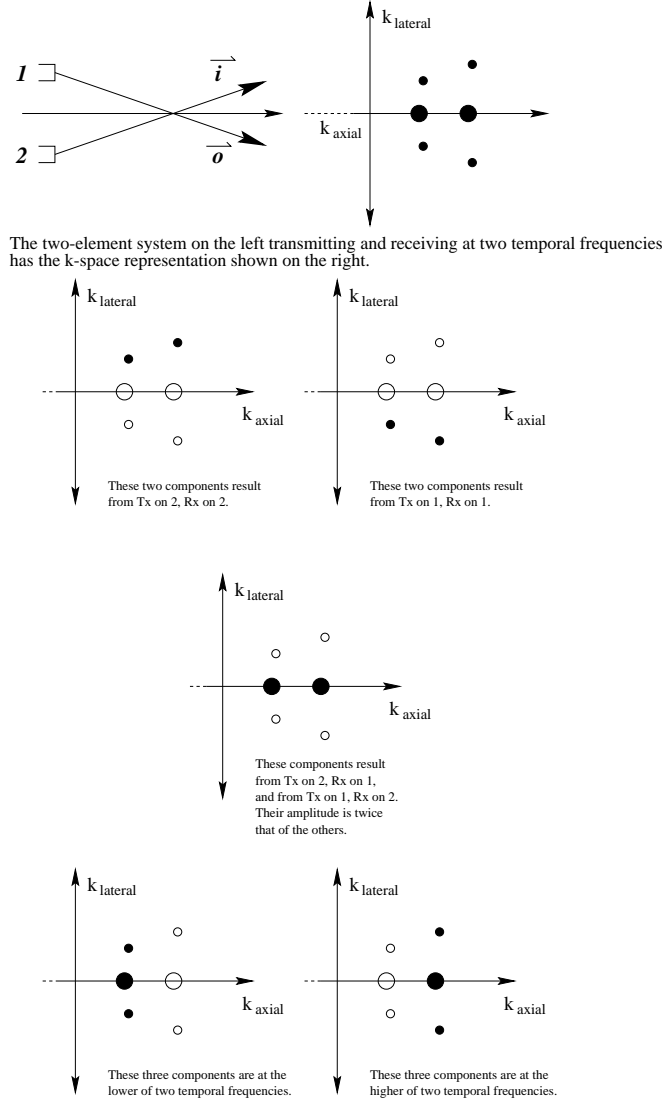
The two-element system on the left transmitting and receiving at two temporal frequencies has the k-space representation shown on the right.

These two components result from Tx on 2, Rx on 2.

These two components result from Tx on 1, Rx on 1.

These components result from Tx on 2, Rx on 1, and from Tx on 1, Rx on 2. Their amplitude is twice that of the others.

These three components are at the lower of two temporal frequencies.

These three components are at the higher of two temporal frequencies.

Figure 3.5: (Top) A two-element system transmitting and receiving on two temporal frequencies (left) has a k-space response with six distinct spatial frequency components (right). (Bottom) These components are also shown separated into five groups in k-space.

3.10. The lateral pulse-echo beam pattern and k-space response is for this aperture are seen to be a product in space and a convolution in frequency of the transmit-only cases, respectively, as shown in Figure 3.11. The axial response is an acoustic pulse that becomes progressively stretched off axis, with interference increasing progressively off axis.

The triangular lateral response is due to the presence of a larger number of elements at close spacing, while a smaller number of elements are placed at large spacing. Hence the weighting of the frequency response reflects the weighting of the sampling of spatial frequencies in the aperture, and is directly related to spatial resolution, as shown in Figure 3.12. The elements at the ends of the array are creating the highest spatial-frequency signals. If you remove the elements from the ends, the spatial frequency response gets narrower. The limited spatial resolution that results is not a sampling effect, but the result of the filtering effect of propagation from a limited aperture.
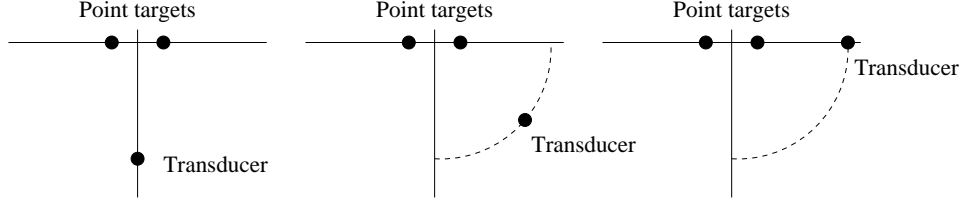
Figure 3.6: A simple point transducer imaging system has axial but no lateral resolution. When two point targets are separated in the lateral dimension only, (left) this system cannot resolve them. By rotating the system through an arc relative to the targets, (center, right) the axial and lateral spatial frequencies of the original transducer/target geometry are exchanged, such that the final orientation (right) allows the targets to be resolved.
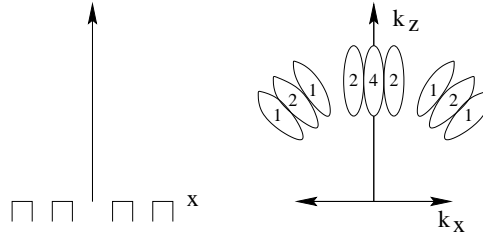

Figure 3.7: A four-element system (left) and its k-space response (right).

Hence this limit is referred to as the **diffraction-limited resolution** of the system. In a typical system with an f-number on the order of 2, the lateral to axial spatial frequency mismatch can be on the order of 10!

3.4 K-space is a two-dimensional frequency space

General principles of k-space analysis:

- Think about the transfer function in two dimensions.

- New surface area is equivalent to new information.

- An ideal imaging system is an all-pass filter.

- A realistic system has an impulse response, or point spread function, the Fourier transform of which is the spatial frequency response in k-space.

- Improvements in the point spread function correspond to a greater region of support in k-space, reflecting an improved capability to gather more information.

For example, if the k-space regions of support of two echo patterns overlap, the patterns themselves will be highly correlated. On the other hand, if they have no overlap, the corresponding speckle patterns will be completely uncorrelated. This is not an approximation, but the equivalent of the correlation operation in two dimensions. It is rigorous within the constraints of the approximation underlying the k-space representation.
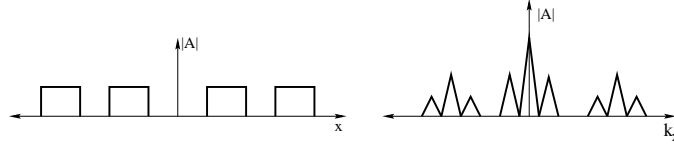
27

Figure 3.8: The lateral k-space response of the four-element system (right) can be approximated by the auto-convolution of its aperture function (left).
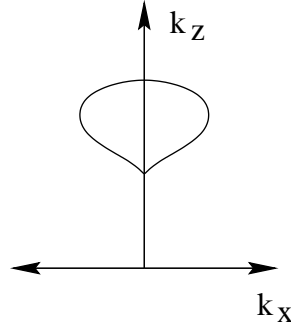

Figure 3.9: In the lateral dimension, the cross-section of this function is a triangle. In the axial dimension, the cross-section is Gaussian.

3.5 Imaging trade-offs

Given the sinc^2-shaped response of a rectangular aperture, we observe a trade-off between lateral resolution and contrast. Commercial machines apodize the aperture to reduce the sampling of high lateral frequency components in the aperture. This reduces spatial resolution but improves contrast by reducing the energy in the side lobes of the sinc^2.

One could attempt to apodize the aperture to increase the sampling of high lateral frequency components in the aperture. This would produce a sharper main lobe, but this improvement in lateral resolution would be offset by a degradation in contrast due to the emphasis of the side lobes. This approach is sometimes used in commercial scanners in a **zoom** mode.

Another trade-off is lateral resolution versus the depth-of-field (DOF). Given $f_\# = z/d$, DOF $= 8\, f_\#^2 \lambda$. Note that this dependence is with the square of the aperture size. As shown in Figure 3.13, the smaller the DOF, the smaller the "sweet-spot" of the transmit response. The DOF can be kept constant on receive by using dynamic aperture growth on receive. On transmit, this can only be achieved by using multiple transmit foci. This reduces the frame rate by a factor proportional to the number of transmit foci.

The k-space examples shown up to this point have been flat phase, but under real conditions there is often has some phase profile across the aperture. This profile may be artificial, e.g. to achieve focusing and steering of the beam, or it may be a natural phase aberration arising from structures in the medium. Ideal focusing achieves perfect superposition of waves at the focus. In a real system, the focus phase profile is quantized. This produces **phase quantization error** at the focus, as shown in Figure 3.14. The magnitude of this error is determined by the transducer geometry and the scanner hardware.

While focusing in the lateral dimension of a 1-D array can be applied electronically, focusing in the elevation dimension is typically achieved with an acoustic lens, which by its nature has a fixed focal
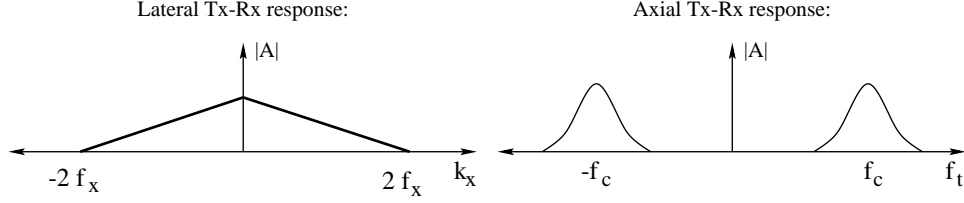
Figure 3.10: An ultrasound system has responses in both lateral (left) and axial (right) spatial frequencies. The axial spatial frequencies are usually presented as temporal frequencies. A typical system has a pass-band axial response centered at the transducer's center frequency, f_c.
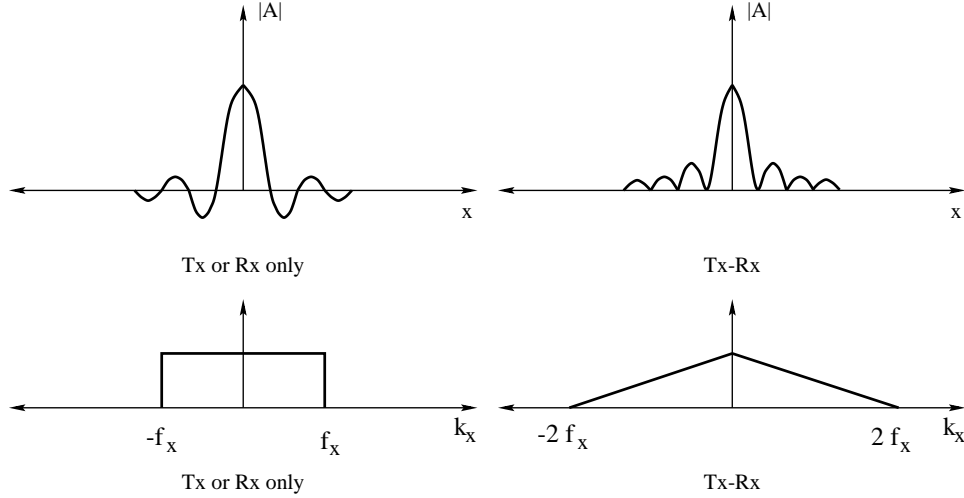

Figure 3.11: (Top) The transmit-only (left) and transmit-receive (right) amplitude in the observation plane of a rectangular aperture. The transmit-only (left) and transmit-receive (right) lateral k-space responses of a rectangular aperture.

length. Acoustic lenses are often quite severe, therefore the depth of field is poor in elevation. As a consequence the elevation dimension spatial resolution can vary by a factor of 10 within a typical range of interest. Clinicians are often not aware of this slice thickness problem.

Annular arrays are well focused in both dimensions, but can only used with mechanical scanners. These types of scanners cannot perform color-flow or simultaneous Doppler/B-mode imaging.

3.6   The target function and scattering:

When considering the pulse-echo response of the system to a scattering function at the focus, the point spread function can be used as a kernel that is convolved with a target function. In k-space the transfer function is multiplied by the spatial frequencies in the target function to produce the image frequency spectrum.

Target structures that scatter with spatial frequencies higher than the extent of the system response are sub-resolution and are not imaged by the system. The k-space representations of target functions are related to their information content. Spatial frequencies in the target function do not represent plate reflectors, but rather are sinusoidal variations in scatterer reflectivity. For example, the glomeruli in the kidney create a ~ 3 cycles/mm pattern. A schematic of this type of scattering
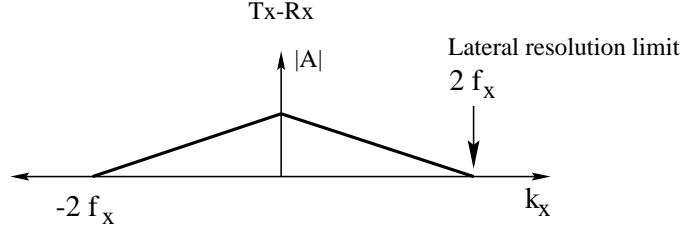
Figure 3.12: The extent of the region of support of the lateral k-space representation of an imaging system defines its lateral spatial resolution.
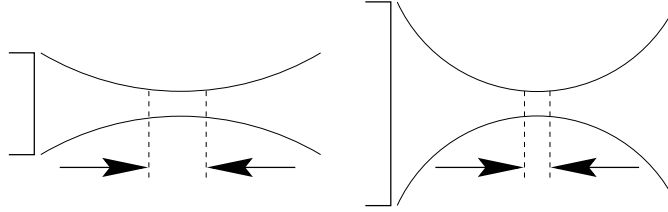

Figure 3.13: The depth of field, indicated by the arrows, is an inverse function of the aperture size.

structure is shown in Figure 3.15. Resolving this structure requires spatial resolution of at least 1/6 mm in the dimension along which the structure's periodicity is oriented.

In k-space this target is represented with an impulse-pair indicating the periodicity of the amplitude variation, as shown in Figure 3.16. In order to see this target with a minimal system, you have to transmit at the same spatial frequency.

With a repeated structure, a **comb** function is produced, as shown in Figure 3.17. If this structure were rotated, one would need to launch the pulse along a similarly rotated axis in order to see the structure.

Given a dominant axial scatterer spacing of a, consider the predicted response of the system, shown schematically in Figure 3.18. Observe that this type of target produces lobes in the echo frequency response. Note that the transmit-receive process introduces a factor of two in the observed axial periodicity, e.g. a dominant scatterer spacing of a in space is observed as a $2a$ spacing in transmit-receive k-space. Periodicity in the scattering function produces periodicity in the echo spectrum. This is the basis of some tissue characterization techniques, e.g. if pathology is correlated with tissue structure at scales to which the imaging system is sensitive, the associated echo spectra may carry useful diagnostic information[14, 15, 16, 17, 18, 19, 20].

3.7 Frequency dependent effects:

Aside from scatterer structure, another factor that affects the target k-space response is attenuation. This functions as a low-pass filter in temporal frequency. Absorption accounts for 98% of ultrasound attenuation, while the remaining 2% arises from scattering. (The imaging process relies on this 2%!) Attenuation is typically frequency dependent, hence the parameter **frequency dependent attenuation** (FDA). The range of typical tissue attenuation values is 0.3-2 dB/cm-MHz. Its impact on the pulse-echo response is shown in Figure 3.19. Note that the fractional bandwidth for a system with a Gaussian temporal frequency response remains the same after attenuation. While the axial
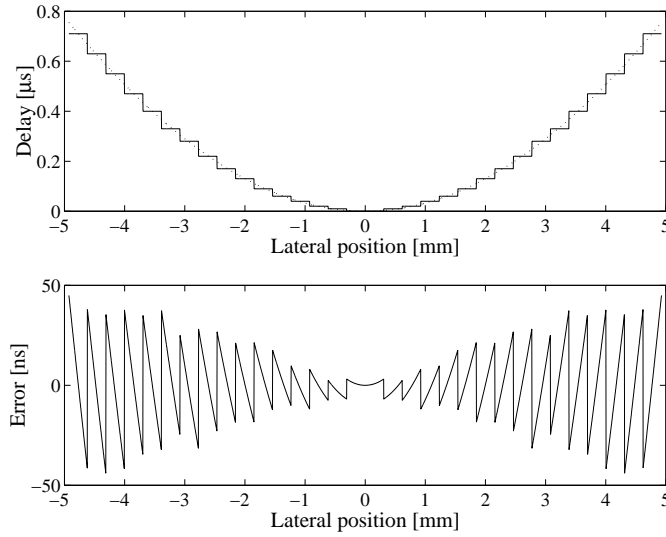
Figure 3.14: (Top) For a 32 element 5 MHz array with element pitch = λ and focused at f/1, the ideal geometric delays across the array are shown by the dotted line. The actual delays achieved with 10 ns delay quantization and given the element size are shown with the solid line. The difference between the ideal and actual delays (bottom) is known as the phase quantization error.

resolution is not affected by attenuation, lateral resolution is degraded.

The echogenicity of tissue also has a frequency dependence that can run counter to frequency dependent attenuation. A Rayleigh scatterer is a scatterer of size $<< \lambda$. This echo intensity from this type of scatterer has an f^4 dependence. This relationship helps the imaging process. For example, in the 1-5 MHz range, the echo from blood is approximately 20 decibels below that from tissue, making imaging and quantification of slow flow difficult. However, in the 20-30 MHz range blood cells become Rayleigh scatterers, such that the echo from blood is as bright as from the tissue.

Finally, the target-array geometry can produce spatial-frequency weighting that is a function of position. More widely-spaced elements see shorter path length differences among scatterers along the beam axis, as shown in Figure 3.20. Therefore scatterers are effectively closer together. Therefore one needs a higher frequency to produce the same axial interference pattern as that observed with elements at the center of the array.

3.8   Tissue anisotropy

A Rayleigh scatterer is perfectly isotropic. Upon isonification, such a scatterer **emits** sound in all directions equally. Large groups of these scatterers can produce a more directed echo pattern. A great number of individual scatterers aligned along a line or surface effectively form a specular reflector, a physical manifestation of the Huygen-Fresnel principle.

A real-world factor not included in our theoretical discussion is the anisotropy of tissue. K-space was in fact first applied in ultrasound to describe tissue anisotropy[1]. Skeletal muscle has strong anisotropy due to its structure, but this type of muscle is a little interest in the ultrasound imaging. Cardiac muscle, on the other hand, shows an anisotropy that changes with both of the location in
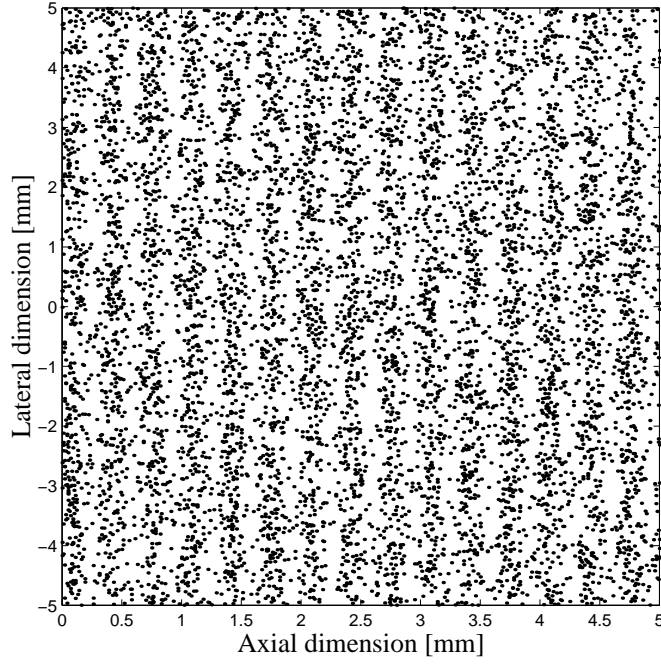
Figure 3.15: A medium having structure with reflectivity modulated at 3 cycles/mm in the axial dimension.
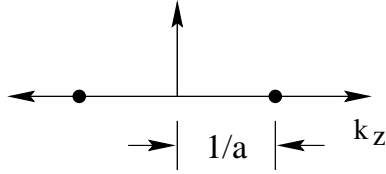
Figure 3.16: A structure with sinusoidally distributed scatterers with a dominant spacing of a will have an impulse-pair k-space representation.

the heart and over the cardiac cycle.

Miller *et. al* [21] have shown that the cyclic variation in backscatter due to this anisotropy is different in healthy versus pathologic cardiac tissue. This is considered a potential means of diagnosis, although it is difficult to apply this method in a controlled manner, as the orientation of the sound beam and of the organ itself affects the results.

Figure 3.17: Generally, a repeated scattering structure (i.e. not strictly sinusoidally distributed) is represented by a **comb** function.
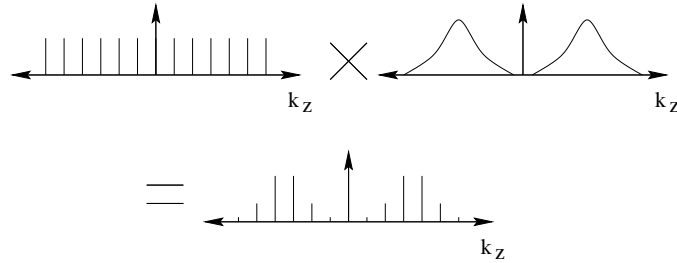
Figure 3.18: Given a dominant axial scatterer spacing of a, the output of the system is the corresponding **comb** function multiplied by the response to the system. Note that the transmit-receive process introduces a factor of two 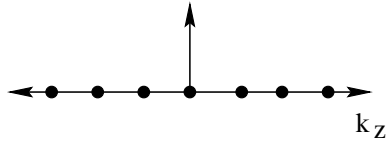in an observed axial periodicity, e.g. a dominant scatterer spacing of a in space is observed as a $2a$ spacing in transmit-receive k-space
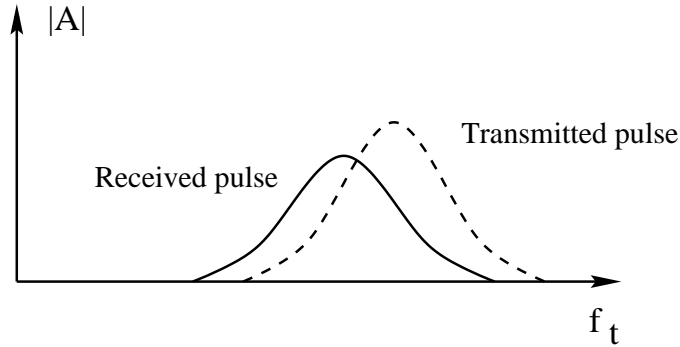
Figure 3.19: Generally, frequency dependent attenuation lowers the center frequency and amplitude of the pulse as it propagates through tissue. Here the temporal frequency content of the transmitted pulse is compared to that of the received echo, showing these effects. (Note that the relative amplitudes of these responses are not drawn to scale.)
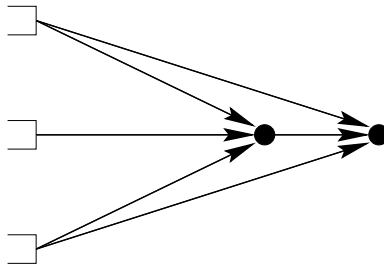
Figure 3.20: In a three element system, the outer elements see an effectively smaller spacing between two on-axis scatterers than the central element. The scattered axial interference pattern observed by central element can only be observed by the outer elements by scaling the interrogation frequency proportionately.

Chapter 4

A beginner's guide to speckle

An inherent characteristic of coherent imaging, including ultrasound imaging, is the presence of speckle noise. Speckle is a random, deterministic, interference pattern in an image formed with coherent radiation of a medium containing many sub-resolution scatterers. The texture of the observed speckle pattern does not correspond to underlying structure. The local brightness of the speckle pattern, however, does reflect the local echogenicity of the underlying scatterers.

Speckle has a negative impact on ultrasound imaging. Bamber and Daft show a reduction of lesion detectability of approximately a factor of eight due to the presence of speckle in the image[22]. This radical reduction in contrast resolution is responsible for the poorer effective resolution of ultrasound compared to x-ray and MRI.

Speckle is present in both RF data and envelope-detected data. In Figure 4.1 we see a simple conceptual demonstration of the impact of speckle noise on information content. The object of interest is a hypoechoic lesion of 5 mm diameter with -9 dB contrast. The echogenicity map corresponding to this object is shown in the top left panel of Figure 4.1, opposite the corresponding scattering function in the top right panel. The scattering function represents the population of sub-resolution scatterers being imaged, and that are weighted in amplitude by the echogenicity map. This scattering function was convolved with the point spread function of a hypothetical 7.5 MHz array (60 % bandwidth, imaging at f/1). The resulting RF echo data is shown in the lower left panel. The RF echo data is zero-mean and thus does not show what is really of interest, i.e. a map of local echogenicity, or local echo magnitude. Envelope detection removes the 7.5 MHz carrier, producing the desired image of echo magnitude in the lower right panel. Here it is easy to see how speckle noise obscures the information in the image. While the mean speckle brightness at each region of the image reflects the original echogenicity map, the speckle noise itself does not reflect the structure, or information, in either the echogenicity map or the corresponding scattering function.

4.1   The statistics of fully-developed speckle

Given the stochastic nature of speckle noise, we must describe this noise pattern statistically to draw general conclusions about imaging systems. The statistics used here to describe ultrasound speckle are drawn from the literature of laser optics[23]. Each of the diffuse scatterers in the isochronous volume contributes a component to the echo signal in a sum known as a **random walk** in the complex plane. This is shown schematically in Figure 4.2. If each step in this walk is considered
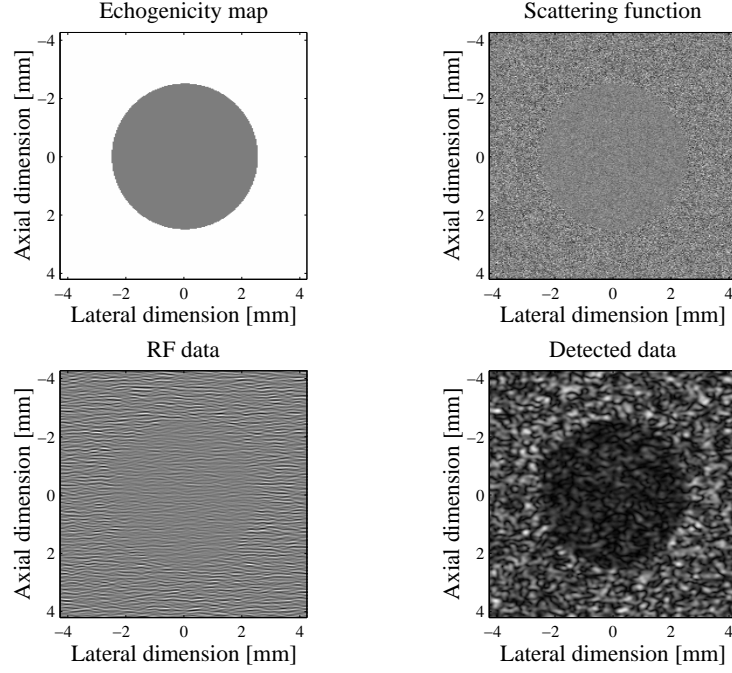
Figure 4.1: The ultrasound image of a hypoechoic lesion of 5 mm diameter with -9 dB contrast is considered. The echogenicity map corresponding to this object is shown in the top left panel, opposite the corresponding scattering function in the top right panel. The scattering function represents the population of sub-resolution scatterers being imaged, and that are weighted in amplitude by the echogenicity map. This scattering function was convolved with a point spread function to produce the RF echo data is shown in the lower left panel. The RF echo data is zero-mean and thus does not show what is really of interest, i.e. a map of local echogenicity, or local echo magnitude. Envelope detection removes the carrier, producing the desired image of echo magnitude in the lower right panel. The differences between this image and the original echogenicity map arise from speckle noise.

an independent random variable, over many such walks we can apply the Central Limit Theorem to their sum. Therefore, in fully developed speckle, this complex radio-frequency echo signal from diffuse scatterers alone has a zero mean, two-dimensional Gaussian probability density function (PDF) in the complex plane.

Envelope detection removes the phase component, creating a signal with a Rayleigh amplitude PDF:

$$p_A(a) = \frac{a}{\sigma^2} exp\left(-\frac{a^2}{2\sigma^2}\right), a \geq 0 \tag{4.1}$$

Speckle brightness is greater if there are fewer, longer steps in the random walk than if there are many shorter steps. This could be accomplished by improving the spatial resolution of the system. On the other hand, if the scatterer density is doubled, a $\sqrt{2}$ increase in brightness results.
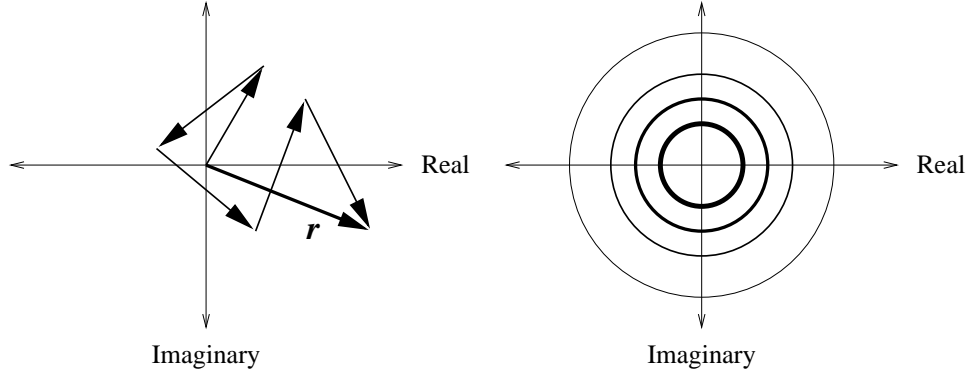
Figure 4.2: (Left) Through superposition, each scatterer in a population of diffuse scatterers contributes an echo signal that adds one step in a **random walk** that constitutes the resulting received complex echo r. (Right) A contour plot of the PDF of r, a 2-D complex Gaussian centered at the origin. The values of the magnitude of r for many such scatterer populations follow the Rayleigh PDF.

4.2 Coherent components and Rician statistics

When a coherent component is introduced to the speckle, it adds a constant strong phasor to the diffuse scatterers echoes and shifts the mean of the complex echo signal away from the origin in the complex plane, as shown in Figure 4.3. Upon detection, this has the effect of changing the Rayleigh PDF into a Rician PDF. The Rician PDF is defined by the following equation:

$$p_A(a) = \frac{a}{\sigma^2} exp\left(-\frac{a^2 + s^2}{2\sigma^2} \right) I_0 \frac{as}{\sigma^2}, a \geq 0 \tag{4.2}$$
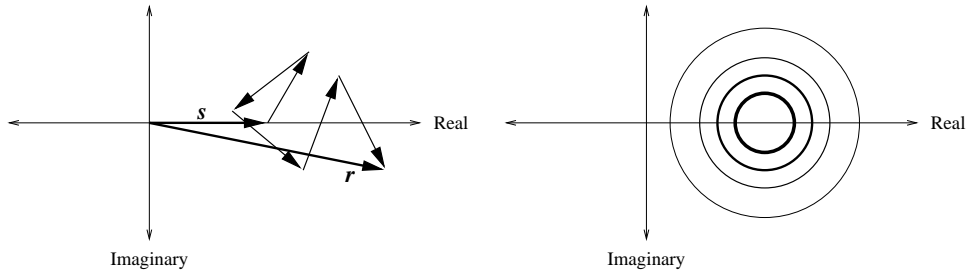
Figure 4.3: (Left) The presence of a coherent component in the scatterer population adds a constant vector s to the random walk. (Right) A contour plot of the PDF of r, a 2-D complex Gaussian centered at the end of s. The values of the magnitude of r for a particular s follow the Rician probability PDF over many different populations of diffuse scatterers.

These PDFs are nonzero for $a \geq 0$ only. The parameter s is the echo strength of the bright scatterer, while σ is the standard deviation of the complex Gaussian described above, i.e. both the real part and the imaginary part have variances of σ. I_0 is the incomplete Bessel function of zero order. The Rician PDF is parameterized by the variable k, which is defined as s/σ[23]. The Rician PDF reduces to the Rayleigh PDF for the special case $s = 0$. A family of Rician PDFs for various values of k, including the Rayleigh PDF, is shown in Figure 4.4.
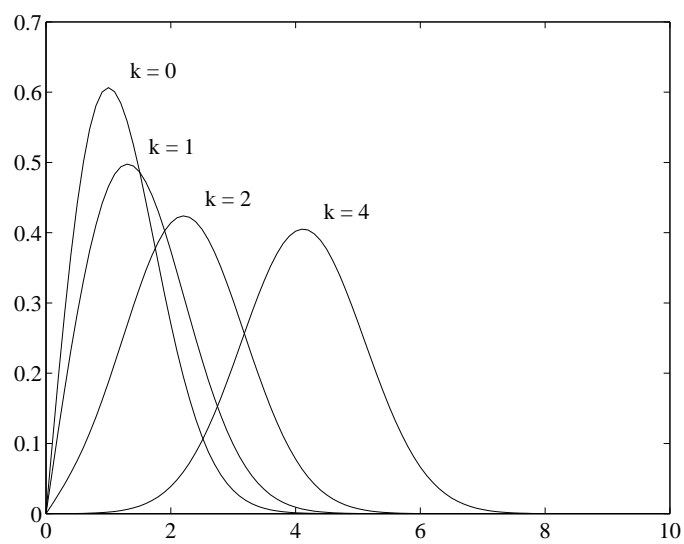
Figure 4.4: The Rayleigh PDF ($k = 0$) and a family of Rician PDFs, parameterized by the variable k.

Chapter 5

First order speckle statistics

5.1 Magnitude (using Trahey's notation)

Given a monochromatic carrier signal described with the phasor form $e^{j2\pi f_c t}$, where f_c is the center frequency, we introduce a formulation of the RF speckle pattern in the analytic form:

$$P(x, y, z; t) = A(x, y, z)e^{j2\pi f_c t} \tag{5.1}$$

where $A(x, y, z)$ is the complex phasor amplitude. $A(x, y, z)$ can be decomposed into magnitude and phase:

$$A(x, y, z) = |A(x, y, z)|e^{j\theta(x,y,z)} \tag{5.2}$$

The intensity of the phasor is given by:

$$I(x, y, z) = |A(x, y, z)|^2 \tag{5.3}$$

Each scatterer contributes to the complex phasor amplitude:

$$A(x, y, z) = \sum_{k=1}^{N} \frac{1}{\sqrt{N}} a_k(x, y, z) = \frac{1}{\sqrt{N}} \sum_{k=1}^{N} |a_k| e^{j\theta_k} \tag{5.4}$$

Assumptions:

- The amplitude $a_k/\sqrt{N}$ and phase θ_k of the kth scatterer are statistically independent of each other and of those of all other scatterers.

- The phases of the scatterers are uniformly distributed over $[-\pi, \pi]$.

Now we can calculate an assortment of expected values:

$$A^r = \text{Real}(A) = \frac{1}{\sqrt{N}} \sum_{k=1}^{N} |a_k| \cos(\theta_k)$$

$$A^i = \text{Imaginary}(A) = \frac{1}{\sqrt{N}} \sum_{k=1}^{N} |a_k| \sin(\theta_k)$$

$$\langle A^r \rangle = \frac{1}{\sqrt{N}} \sum_{k=1}^{N} \langle |a_k| \cos(\theta_k) \rangle = \frac{1}{\sqrt{N}} \sum_{k=1}^{N} \langle |a_k| \rangle \langle \cos(\theta_k) \rangle = 0$$

$$\langle A^i \rangle = \frac{1}{\sqrt{N}} \sum_{k=1}^{N} \langle |a_k| \sin(\theta_k) \rangle = \frac{1}{\sqrt{N}} \sum_{k=1}^{N} \langle |a_k| \rangle \langle \sin(\theta_k) \rangle = 0$$

$$\langle |A^r|^2 \rangle = \frac{1}{N} \sum_{k=1}^{N} \sum_{m=1}^{N} \langle |a_k a_m| \rangle \langle \cos(\theta_k) \cos(\theta_m) \rangle = \frac{1}{N} \sum_{k=1}^{N} \frac{\langle |a_k| \rangle^2}{2}$$

$$\langle |A^i|^2 \rangle = \frac{1}{N} \sum_{k=1}^{N} \sum_{m=1}^{N} \langle |a_k a_m| \rangle \langle \sin(\theta_k) \sin(\theta_m) \rangle = \frac{1}{N} \sum_{k=1}^{N} \frac{\langle |a_k| \rangle^2}{2}$$

$$\langle A^r A^i \rangle = 0$$

(5.5)

Through the application of the Central Limit Theorem, $A(x, y, z)$ has a complex Gaussian PDF, with joint real and imaginary parts:

$$p_{r,i}(A^r A^i) = \frac{1}{2\pi\sigma^2} \exp\left(-\frac{|A^r|^2 + |A^i|^2}{2\sigma^2} \right)$$

$$\text{where } \sigma^2 = \lim_{N \to \infty} \frac{1}{N} \sum_{k=1}^{N} \frac{|a_k|^2}{2}$$

(5.6)

For large N the Rayleigh PDF of the phasor magnitude is found to be:

$$p(V) = \begin{cases} \frac{V}{\sigma^2 N} \exp\left(-\frac{V^2}{2\sigma^2 N} \right) & V \geq 0, \\ 0 & \text{otherwise.} \end{cases}$$

(5.7)

The first order statistics for magnitude are:

$$\mu_V = \langle V \rangle = \left(\frac{N\pi}{2} \right)^{1/2} \sigma$$

$$\sigma_V^2 = \langle (V - \mu)^2 \rangle = [2 - \pi/2] N \sigma^2$$

$$\therefore \mu_V / \sigma_V = 1.91, \text{ equivalent to 5.6 dB SNR}$$

(5.8)

5.2   Intensity (using Goodman's notation)

$|A(x, y, z)|^2$ has the PDF:

$$p(I) = p(V^2) = \begin{cases} \frac{1}{2\sigma^2} \exp\left(-\frac{I}{2\sigma^2} \right) & I \geq 0, \\ 0 & \text{otherwise.} \end{cases}$$

(5.9)

and statistics:
$$\sigma_I = \mu_I = 2\sigma^2$$

5.3   A review of random variables

Given two random variables x and y:

$$\text{The mean of } x = \mu_x = \langle x \rangle$$

$$\text{where } \langle \rangle \text{ denotes "expected value of".}$$

$$\text{The variance of } x = \sigma_x^2 = \left\langle (x - \mu_x)^2 \right\rangle$$

$$\text{For } x \text{ zero-mean, } \sigma_x^2 = \langle x^2 \rangle$$

$$\text{The standard deviation of } x = \sigma_x$$

$$\text{The covariance of } x \text{ and } y = \mathbb{C}_{x,y} = \left\langle (x - \mu_x)(y - \mu_y)^* \right\rangle \tag{5.10}$$

$$\text{The normalized correlation coefficient of } x \text{ and } y = \rho = \frac{\mathbb{C}_{x,y}}{\sigma_x \sigma_y}$$

$$\mu_{x+y} = \mu_x + \mu_y$$

$$\sigma_{x+y}^2 = \sigma_x^2 + \sigma_y^2 + 2\rho\sigma_x\sigma_y$$

$$\text{For } x, y \text{ independent, } \sigma_{x+y}^2 = \sigma_x^2 + \sigma_y^2$$

$$\text{For } x, y \text{ independent, } \langle xy \rangle = \langle x \rangle \langle y \rangle$$

Chapter 6

Second Order Speckle Statistics

6.1 Speckle and the phase spectrum

At the focus, we consider the phase of k-space response of the ultrasound system to be flat. If we multiply this flat phase k-space response by the complex spectrum of speckle, we observe no net change in the amplitude spectrum, but the phase spectrum takes on the characteristics of the speckle, as shown in Figure 6.1. The phase and amplitude characteristics of the transmit, scattering, and receive events can be represented as three random walks in complex amplitude space. The randomization of phase in any of these walks results in the production of a speckle pattern.

It is also important to note that the randomization of phase shown in Figure 6.1 can also be produced by phase errors or phase aberration in either the aperture function or the propagation
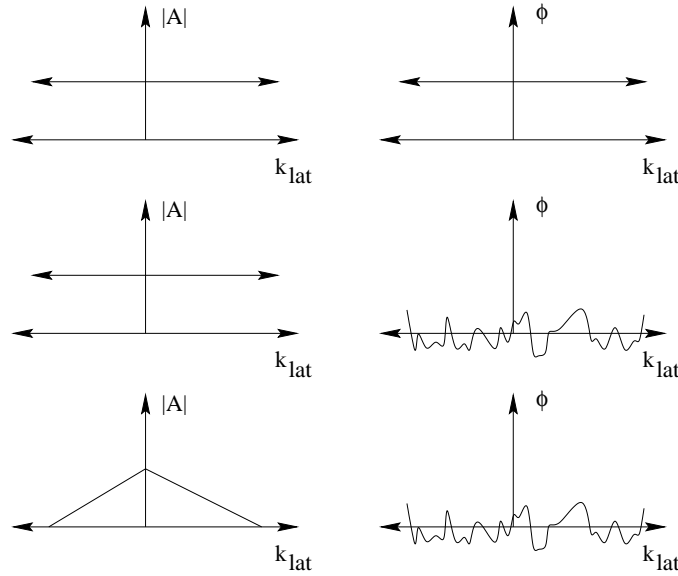

Figure 6.1: The complex spectra for a point target (top) and for a speckle target (middle) in the lateral k-space dimension. The observed (imaged) speckle pattern (bottom) reflects the spatial frequency response of the imaging system.

path. In this manner, it is possible for a point target that has flat phase to appear as a localized speckle pattern to the imaging system, as its echo has taken on the phase characteristics of speckle across the aperture.

6.2 The autocorrelation of speckle

In considering the autocorrelation operation applied to speckle, recall that the power spectrum is the Fourier transform of the autocorrelation operation, and that neither function has a phase component. Therefore, we expect in the autocorrelation functions of a point target (that has a target spectrum with flat phase) and a speckle pattern (that has a target spectrum with random phase) to be the same in both lateral and axial dimensions, since the autocorrelation function is phase independent. These functions for RF and detected speckle signals are shown in Figure 6.2.
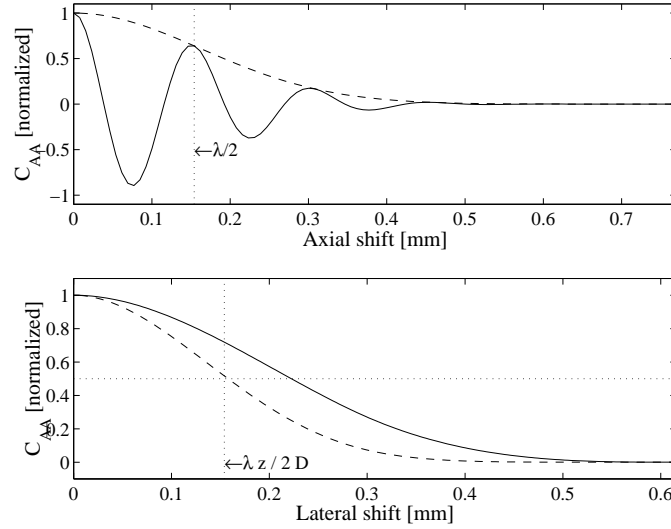

Figure 6.2: The autocorrelation functions of the RF signal (solid line) and the detected signal (dashed line) for the axial (top) and lateral (bottom) dimensions.

Any power spectrum or autocorrelation function estimated from a limited window of speckle data will have random fluctuations due to the stochastic nature of the speckle pattern. Thus when these functions are actually estimated from speckle data, one must average over many independent realizations of the speckle to produce the expected result.

The ringing in the autocorrelation function of the original RF echo signal means that its main lobe width cannot be used as a meaningful index of spatial resolution. There is no ringing in the lateral dimension.

The widths of the detected signal's lateral and axial autocorrelation functions reflect the system resolution in these dimensions. We use the following rules of thumb:

- lateral resolution = $\lambda z / D$

- axial resolution $\approx \frac{1}{2}$ pulse length ($\approx \lambda$ for 100% relative bandwidth)

In general, lateral resolution is worse than axial resolution, and gets worse with range. Therefore,

the system resolution is anisotropic. Given the Gaussian axial spatial frequency response and typical attenuation, the shape of the echo envelope remains constant. Thus axial resolution is constant over range even though the echo pulse's mean frequency decreases.

6.3 Important speckle references:

The speckle statistics presented here follow Goodman[23]. Another good source on laser optics is also by Goodman[24]. The first discussion of ultrasound speckle using statistical optics is in Burckhardt[25]. Advanced papers on the statistics of speckle include Wagner, *et al.*[26] and Thijssen, *et al.*[27]. A classic paper on the second-order statistics of speckle is by Wagner, *et al.*[28]. The effect of aberration on speckle statistics is discussed in Trahey and Smith, *et al.*[29, 30]. A discussion of Rician statistics in tissue characterization is in Insana, *et al.*[17]. There are many sources on compounding. Several sources include investigations of spatial compounding in Trahey and O'Donnell, *et al.*[31, 32] and of frequency compounding Melton and Trahey [33, 34].

Chapter 7

Spatial and temporal coherence

The concepts of spatial and temporal coherence are important in discussing the phase characteristics of imaging systems. In general, the concept of coherence is related to the stability, or predictability, of phase.

Spatial coherence describes the correlation between signals at different points in space. Temporal coherence describes the correlation or predictable relationship between signals observed at different moments in time.

Spatial coherence is described as a function of distance, and is often presented as a function of correlation versus absolute distance between observation points $\rho_{AB}(|x_1 - x_2|)$. If $\langle P(x_1)P(x_2)\rangle = 0$, there is no spatial coherence at $|x_1 - x_2|$, i.e. $\rho_{AB}(|x_1 - x_2|) = 0$.

The same operation can be performed in time with the results plotted as correlation versus relative delay τ. For the echo signal over the ensemble, temporal correlation is periodic at the inverse of the pulse repetition frequency (1/PRF), as shown in Figure 7.1. This holds for both transmit and receive, and for a point target or a speckle target.

The temporal correlation length of pulsed ultrasound is typically on the order of 1 μs, and in the case of repeated interrogation, is periodic. Therefore the speckle target looks the same on each interrogation. For incoherent radiation, there is no temporal coherence on the order of the pulse repetition interval. All radiation has some finite correlation length.

If you capture an image within the correlation length, you get a single speckle pattern. Laser light has a temporal correlation length on the order of seconds, therefore one can observe stable speckle patterns from scattering functions illuminated with laser light. Images captured at different times with incoherent radiation are uncorrelated, and are averaged in the final image if viewed with a detector whose response time is longer than the finite correlation length.

The spatial correlation of echoes from a point target is constant. For a speckle target, the VCZ curve takes over. (If this were not the case, spatial compounding would have no effect.) Propagation is a low pass filter, therefore we expect the spatial correlation length to increase with distance from the source.

The spatial coherence of the radiation falling on a surface can be measured by changing the spacing between the two openings in the surface at p_1 and p_2, and observing the interference pattern that is generated on a screen beyond, as shown in Figure 7.2. If the pattern dies out after the first fringe, the temporal coherence is on the order of one wavelength. For laser light, the interference pattern is very wide. If intensity patterns of **incoherent** radiation could be detected within its
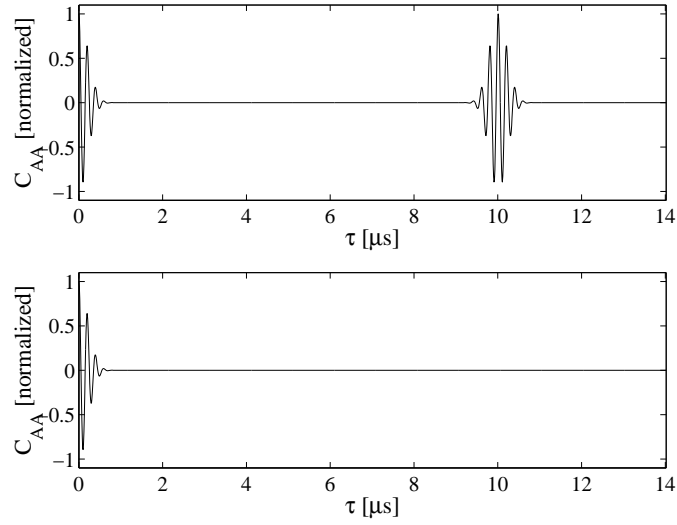
Figure 7.1: (Top) Under multiple interrogations of a target with coherent radiation, the temporal correlation of the echo has periodicity within a pulse length and also at the pulse repetition interval. (Bottom) **Incoherent** radiation typically exhibits some finite correlation, but only within the pulse length.

very short temporal correlation length, then the fringe pattern would extend out to infinity. Over many events, averaging flattens out this extended pattern. Assuming some type of averaging is occurring, often in the detector, only waves with some finite coherence will interfere. In optics using an intensity detector, the number of averaged images approaches infinity. The width of the interference pattern tells us about the temporal and spatial coherence of the radiation.
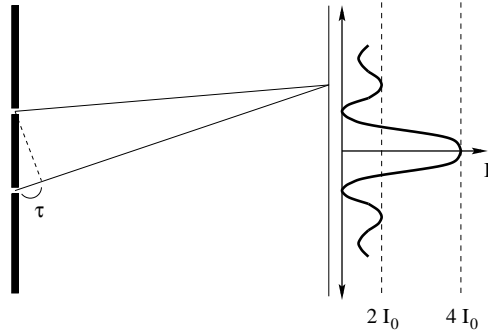
Figure 7.2: Schematic of the Michelson interferometer, in which the intensity pattern cast on a screen by a dual-slit aperture is used to determine the temporal coherence length of the incident radiation. Only coherent radiation creates an interference pattern. Given an mean incident intensity at the screen of I_0, perfect constructive interference produces an intensity of $4I_0$.

In optics, temporal coherence is also measured by combining beams from the same source but having a known path length difference, and observing the interference pattern produced. This path length difference is achieved using a beam splitter, as shown in Figure 7.3.
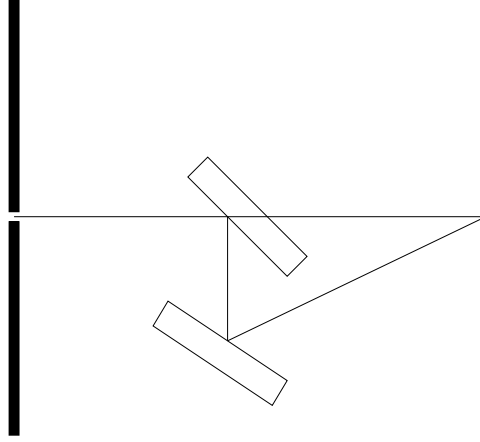
Figure 7.3: Schematic of a beam-splitter interferometer, in which the intensity pattern cast on a screen by interfering beams traveling along different path lengths can be used to determine the temporal coherence length of the incident radiation.

7.1 The correlation coefficient in k-space

The normalized correlation coefficient is the cross correlation function adjusted to remove effects related to the energy in the signals. This coefficient is often designated by the variable ρ. Given two random variables x and y, the continuous time expression for $\rho_{x,y}$ is:

$$\rho_{x,y} = \frac{\int_{-\infty}^{\infty}(x - \mu_x)(y - \mu_y)^* \; dt}{\sqrt{\int_{-\infty}^{\infty}(x - \mu_x)^2 \; dt \int_{-\infty}^{\infty}(y - \mu_y)^2 \; dt}} \tag{7.1}$$

As reviewed in Section 5.3, we can simplify this expression using that for variance. Here $\langle \rangle$ denotes "expected value of":

$$\text{The mean of } x = \mu_x = \langle x \rangle$$
$$\text{The variance of } x = \sigma_x^2 = \langle (x - \mu_x)^2 \rangle$$
$$\text{For } x \text{ zero-mean, } \sigma_x^2 = \langle x^2 \rangle$$
$$\text{The standard deviation of } x = \sigma_x$$

$$\text{The covariance of } x \text{ and } y = \mathbb{C}_{x,y} = \langle (x - \mu_x)(y - \mu_y)^* \rangle$$
$$\text{The normalized correlation coefficient of } x \text{ and } y = \rho = \frac{\mathbb{C}_{x,y}}{\sigma_x \sigma_y} \tag{7.2}$$
$$\mu_{x+y} = \mu_x + \mu_y$$
$$\sigma_{x+y}^2 = \sigma_x^2 + \sigma_y^2 + 2\rho\sigma_x\sigma_y$$
$$\text{For } x, y \text{ independent, } \sigma_{x+y}^2 = \sigma_x^2 + \sigma_y^2$$
$$\text{For } x, y \text{ independent, } \langle xy \rangle = \langle x \rangle \langle y \rangle$$
$$\therefore \text{ For } x, y \text{ independent, } \rho_{x,y} = 0$$

The correlation coefficient goes as the cosine between two vectors. "Half-way," the correlation has a value of $0.707 = \sqrt{2}$.

The covariance definition of spatial coherence:

$$\mathbb{C}_{P_1,P_2}(P_1, P_2, \tau) = \langle \mu(P_1, t+\tau)\mu^*(P_2, t) \rangle \tag{7.3}$$

Given stationarity:

$$\mathbb{C}_{P_1,P_2}(P_1, P_2, \tau) = \mathbb{C}_{P_1,P_2}(|P_1 - P_2|, \tau) \tag{7.4}$$

In Goodman this is referred to as the "mutual coherence function"[12].

The covariance definition of temporal coherence:

$$\mathbb{C}_{P_1}(P_1, \tau) = \langle \mu(P_1, t+\tau)\mu^*(P_1, t) \rangle \tag{7.5}$$

For the averaging of intensity patterns, as in compounding:

$$I_{1+2} = I_1 + I_2 + 2\rho_{1,2}\sqrt{I_1 I_2} \tag{7.6}$$

As shown in Figure 7.2, given $I_1 = I_2$,

$$\text{If } \rho = 1, I = 4I_1$$
$$\text{If } \rho = -1, I = 0 \tag{7.7}$$
$$\text{If } \rho = 0, I = 2I_1$$

Consider the vector notation $\vec{V}_1$ and $\vec{V}_2$ for the complex instantaneous amplitudes of two signals separated in phase by the angle ϕ:

$$|\vec{V}_{1+2}|^2 = |\vec{V}_1|^2 + |\vec{V}_2|^2 + 2|\vec{V}_1||\vec{V}_2|\cos\phi \tag{7.8}$$

Using these equations to calculate the effect of spatial compounding on the signal-to-noise ratio (SNR). The compounding of two uncorrelated images produces an SNR improvement of $\sqrt{2}$.

$$\mathbb{G}(f) = \lim_{T\to\infty} \frac{|\nu_T(f)|^2}{T}$$
$$\text{where } \nu_T(f) = \int_T^T x(t)\exp(j2\pi ft)\,dt \tag{7.9}$$

In this terminology, Parseval's theorem is expressed:

$$\int_{-\infty}^{\infty} x(t)x^*(t)\,dt = \int_{-\infty}^{\infty} |\nu_T(f)|\,df \tag{7.10}$$

in which phase information has been lost through conjugate multiplication.

The power spectral density of the output of a random process is the squared modulus of the transfer function of linear system times the power spectrum density of the input random process:

$$\mathbb{G}_{output}(f) = |H(f)|^2 \mathbb{G}_{input}(f) \tag{7.11}$$

The cross correlation function and cross spectral density function are Fourier transform pairs:

$$\mathbb{G}_(f) = |H(f)|^2 \mathbb{G}_{input}(f) \tag{7.12}$$

Neither contains meaningful phase information, and each contains equivalent information.

If we know the k-space windows of a system and target function, or two different windows of the system under compounding, the product of these windows gives the correlation between their echo signals.

The cross spectrum density is a measure of the similarity of two signals at each complex frequency:

$$\mathbb{G}_{u,v}(f) = \int_{\infty}^{\infty} \mathbb{C}_{u,v}(f) \exp(j2\pi f t) \ dt \tag{7.13}$$

In terms of two complex signals $u(t)$ and $v(t)$ and their transforms $U(f)$ and $V(f)$,

$$\mathbb{G}_{u,v}(f) = \lim_{T\to\infty} \frac{\langle U_T(f) V_T^*(f) \rangle}{T} \tag{7.14}$$

The limit as $T \to \infty$ is required to generalize this expression to include functions that do not have analytical Fourier transforms.

This function is a measure of spectral similarity at each frequency:

$$\mathbb{C}_{u,v}(\tau) = \int_{-\infty}^{\infty} \mathbb{G}_{u,v}(f) \exp(-j2\pi f \tau) \ df \tag{7.15}$$

For u, v having equal phase profiles, $G_{uv}(f)$ is a purely real number due to the conjugate operation. For unequal phase profiles, this quantity will be complex and exhibit interference patterns.

Integration of the k-space overlap gives the correlation coefficient at $\tau = 0$:

$$\rho_{u,v}(0) = \frac{\int_{-\infty}^{\infty} \mathbb{G}_{u,v}(f) \ df}{\sqrt{\int_{-\infty}^{\infty} |U(f)|^2 \ df \int_{-\infty}^{\infty} |V(f)|^2 \ df}} \tag{7.16}$$

Envelope detection shifts the signal band to base band, losing the carrier frequency. Ideally, everything but the carrier frequency is preserved, e.g. axial and lateral bandwidth are preserved. The $\rho_{u,v}(0)$ of the detected signals is the square of $\rho_{u,v}(0)$ of the corresponding RF signals.

Chapter 8

Speckle reduction techniques

By translating the k-space window developed by the imaging system, more information can be gathered from the target spatial frequency space. If such translation is used to develop multiple windows in image k-space, the correlation among these windows is proportional to their geometric overlap. The averaging of the detected speckle patterns from such shifted windows in k-space is a means of reducing speckle noise, and is achieved through **spatial** or **frequency compounding**. The correlation coefficient among the k-space windows will tell us if compounding will reduce the speckle. (If the original spectra are in phase, the correlation coefficient is proportional to overlap. This is the case under ideal conditions, i.e. at the focus and with no aberration.)

8.1 Spatial compounding

The transducer-target geometry affects the spatial frequencies in the target function that are interrogated by the imaging system. The effect of movement of either relative to the other is shown in Figure 8.1. Spatial compounding is achieved by the translation of the aperture, as shown in Figure 8.2. The detected signals acquired at different aperture positions are averaged together.
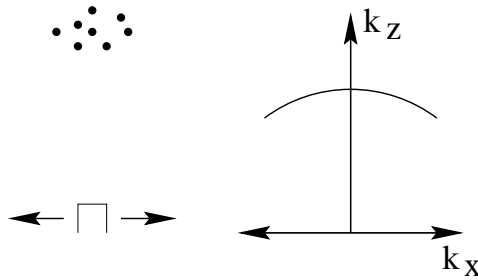

Figure 8.1: If you move a single element with respect to a fixed group of scatterers, you sweep out an arc in k-space.

In a classic paper on speckle second-order statistics by Wagner, *et al.*, we read that the lateral spatial correlation of speckle is equal to the autocorrelation of a triangle function[28]. Translation of one aperture length takes the cross correlation curve to 0, and hence produces statistically independent speckle patterns, but even translation of only 1/4 aperture length reduces the cross correlation function to a very low value, as shown in Figure 8.3.
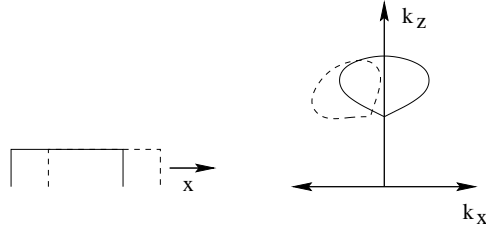
Figure 8.2: Under spatial compounding, the aperture is translated laterally (left) between inter-rogations of the same region of interest. This shifts the system's region of support in k-space, reflecting decorrelation of the response, and hence of the observed speckle patterns. The region of overlap (shaded) is proportional to the correlation between the two speckle patterns.
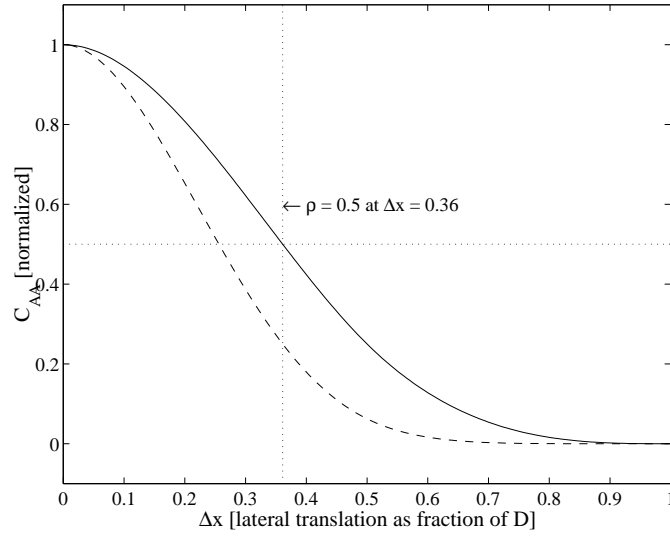

Figure 8.3: As the sub-apertures of a 2:1 spatial compounding system are separated in space, the normalized correlation of the signals received by them changes as a function of this separation.

8.2 Frequency compounding

Frequency compounding adds together detected data from different frequency bands. These frequency bands have different regions of support in k-space, as shown in Figure 8.4.

A simple frequency compounding method is to transmit a single broad bandwidth pulse and to then select different receive frequency "sub-bands" through the application of filters, as shown in Figure 8.5. The axial resolution is now determined by the smaller bandwidth of these compounding filters. This represents a trade-off between speckle SNR and axial resolution.

Again, the correlation between sub-bands is a function of their overlap. Completely discrete bands have no correlation. The signal-to-noise ratio will be different in each band, thus "pre-whitening" filters may be used to level off each band, although doing so amplifies portions of the noise spectrum.

Each sub-band typically has a Gaussian profile axially. Therefore as we change center frequencies of the compounding bands and calculate their cross correlation, we are calculating the autocorrelation function of a Gaussian. For a frequency compounding system, the correlation coefficient between sub-band speckle patterns as a function of the separation of sub-bands is thus the autocorrelation
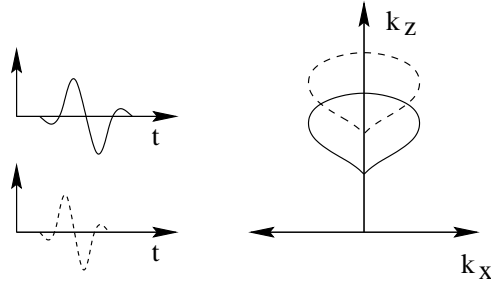
Figure 8.4: Under frequency compounding, the temporal frequency band used in imaging is altered among different interrogations of the same region of interest (left). This shifts the system's region of support along the k_z dimension in k-space, reflecting decorrelation of the response, and hence of the observed speckle patterns. The region of overlap is proportional to the correlation between the two speckle patterns.
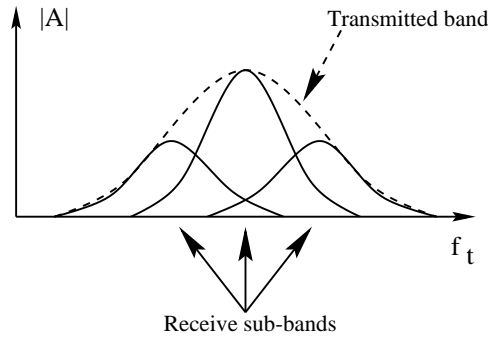

Figure 8.5: Under frequency compounding, a broad temporal frequency band is used on transmit. The receive signal is filtered to produce several receive sub-bands (3, in the diagram above.) Frequency compounding relies on detection of these sub-bands before summation, which averages the partially-uncorrelated speckle patterns they produce. The region of sub-band overlap is proportional to the correlation between the speckle patterns.

function of a Gaussian.

Note that frequency compounding only works on detected data. Averaging RF signals is simply superposition, which recreates the original bandwidth system but achieves no compounding.

Trahey and Smith investigated the speckle reduction vs. spatial resolution trade-off using an expression for lesion detectability based on in contrast-detail study. This work suggested that it is better to use the entire bandwidth coherently.

On the other hand, there is reason to believe commercial scanners are routinely using frequency compounding. This reflects the fact that the axial resolution of a typical scanner's display monitor is not capable of exhibiting the true axial resolution of the system. Given this "excess" of axial resolution, frequency compounding can be applied without an apparent penalty in axial resolution. This cannot be done when the scanner is operated in a "zoom" mode.
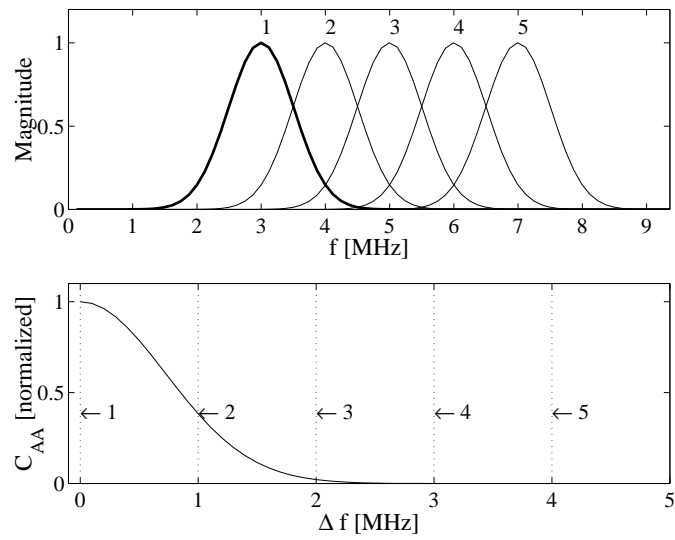
Figure 8.6: As the bands of two receive filters are separated (top), the normalized correlation of the signals received by them changes as a function of the separation in center frequency (bottom).

Chapter 9

Additional topics

9.1 Phase aberration

The spatial and contrast resolution of medical ultrasound can be severely limited by a phenomenon known as phase aberration. The steering and focusing of an ultrasound beam using a phased array relies on an approximation of the speed of sound in tissue, usually 1540 m/s. In fact, the speed of sound through different tissues can vary greatly. As an acoustic wavefront passes through inhomogeneous tissues, it can become distorted as portions of its surface are advanced or retarded. On transmit this phenomenon affects the focusing and steering of the system point spread function (PSF). The returning echoes incident on the elements of the transducer array are also misaligned such that when these signals are summed to form a single echo line they no longer sum coherently, resulting in focal and steering errors, and consequently, diminished echo amplitude.

The discussion is separated into two separate sections, on "first" and "second" order aberrators. In this terminology, first order refers to geometric focal errors due to the difference between the actual mean sound speed in the tissue and that assumed by the ultrasound scanner beamformer. Second order aberration refers to the effects of the inhomogeneity of the tissue that still remain after the first order focal error is removed. Both types of aberration result in blurring of the point spread function and consequently the reduction of spatial and contrast resolution.

A first order aberrator arises from a gross sound speed error in the ultrasound system beamformer relative to the actual tissue, and is usually caused by the application of a single assumed tissue sound speed to all patients. For example, the first order aberration resulting from a 5% overestimation of sound speed is shown in Fig. 9.1. The impact of this aberrator on the system point spread function is shown in Fig. 9.3. In this example, the aberrator was applied to the element delays of a typical array at the f/1 focal range (7.5 MHz, 60% relative bandwidth, 128 elements of width equal to the 1540 m/s wavelength, f/8 in elevation) in an acoustic field simulation program[3]. The aberration leads to an 85% reduction in the PSF energy and a 75% reduction in its peak amplitude. The lateral resolution has been degraded by a factor of 3.9.

An example of a second order aberrator is shown in Fig. 9.2. The impact of this aberrator on the system point spread function is shown in in Fig. 9.4. Once again, this aberrator was applied to the element delays of a typical array (7.5 MHz, 60% relative bandwidth, 128 elements of width equal to the wavelength, f/8 in elevation) in an acoustic field simulation program[3]. The aberration produces an 95% reduction in the PSF energy and a 91% reduction in its peak amplitude. The lateral resolution in this case has been degraded by a factor of 2.3.
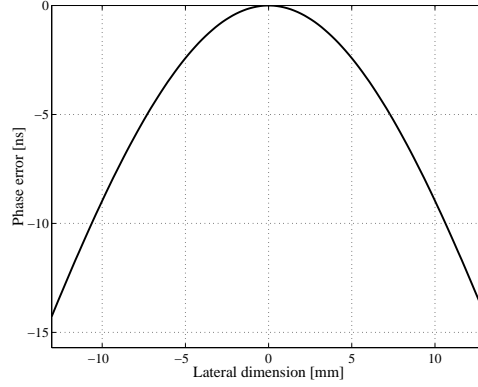
Figure 9.1: The first order phase aberration corresponding to a 5% overestimation in sound speed at the f/1 focal range.

A variety of techniques have been proposed to compensate for the effects of phase aberration[35, 36, 37, 38, 39, 40, 41, 42, 43, 44, 45]. Ideally, the estimated aberrator should be applied on both transmit and receive, as the phase screen affects wave propagation on both transmit and receive.
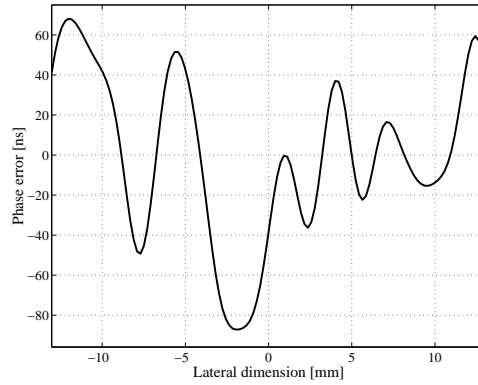

Figure 9.2: One realization of a simulated 50 ns RMS second order aberrator with a spatial auto-covariance FWHM of 3 mm. This particular aberrator creates 41.5 ns RMS phase error across the array, and has a spatial autocovariance FWHM of 2.7 mm.

9.2 The Van Cittert-Zernicke theorem

Speckle has a finite correlation length due to aperture-scatterer path length differences that distinguish one aperture position from another. A point target as infinite correlation length due to the lack of such path length differences.

The Van Cittert-Zernicke theorem states that for an incoherent, diffuse source, the receive spatial correlation function is equal to the Fourier transform of the intensity pattern of the incoherent source[46]. Speckle is a truly incoherent source. The location of scatterers on one line is uncorrelated with that of those in the next.

Cross-correlation methods[47] are affected by VCZ. The VCZ curve falls off even faster in the
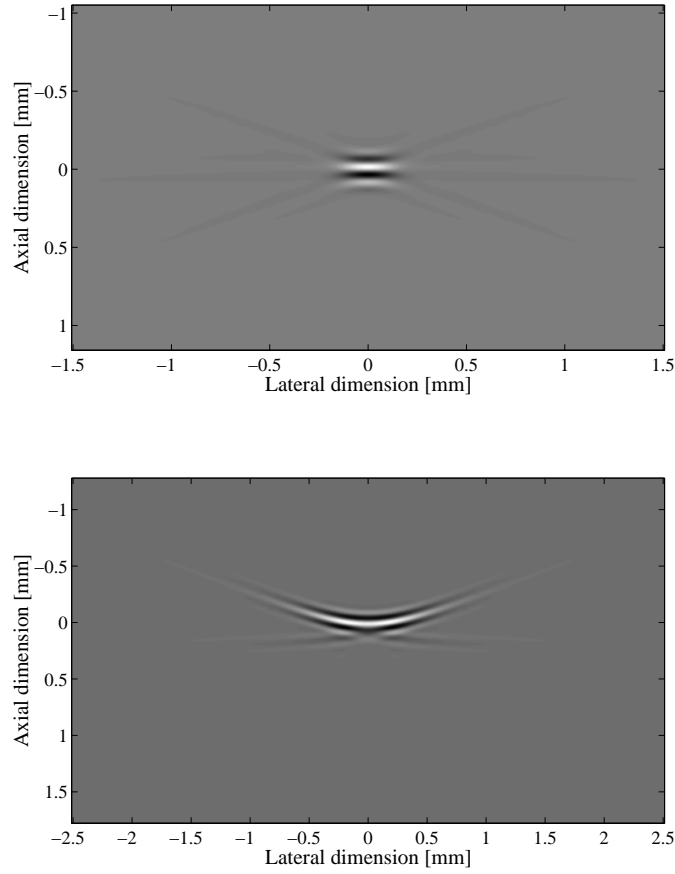
Figure 9.3: The impact of the first order aberrator (sound speed error) shown in Fig. 9.1 on the system point spread function. The aberrated case (bottom) is compared to the unaberrated control (top). The "sharpness" of the PSF is markedly reduced, reflecting losses of spatial and contrast resolution. The images are not displayed with the same gray-scale, so they do not show the 75% reduction in PSF amplitude that the aberration causes.

presence of a transmit phase aberrator due to be broadening of the beam, which scales in k-space to a narrower intensity pattern, thereby producing a steeper correlation curve.

9.3 Deconvolution and super resolution methods

Deconvolution or "super-resolution" methods rely mainly on two approximations. The first of these is known as the Born approximation, which disregards echoes reduced by multiple scattering from targets. The second is that the point spread function is accurately known throughout the region of interest.

Under ideal conditions, deconvolution can work very well. This implies that the noise is very low and that the number of targets is relatively small. Deconvolution does not work well for larger numbers of targets under conditions of low signal-to-noise ratio, especially away from the focus and/or in the presence of phase aberration or attenuation. There performance is also degraded when physical conditions reduce the stationarity of the system's point spread function.
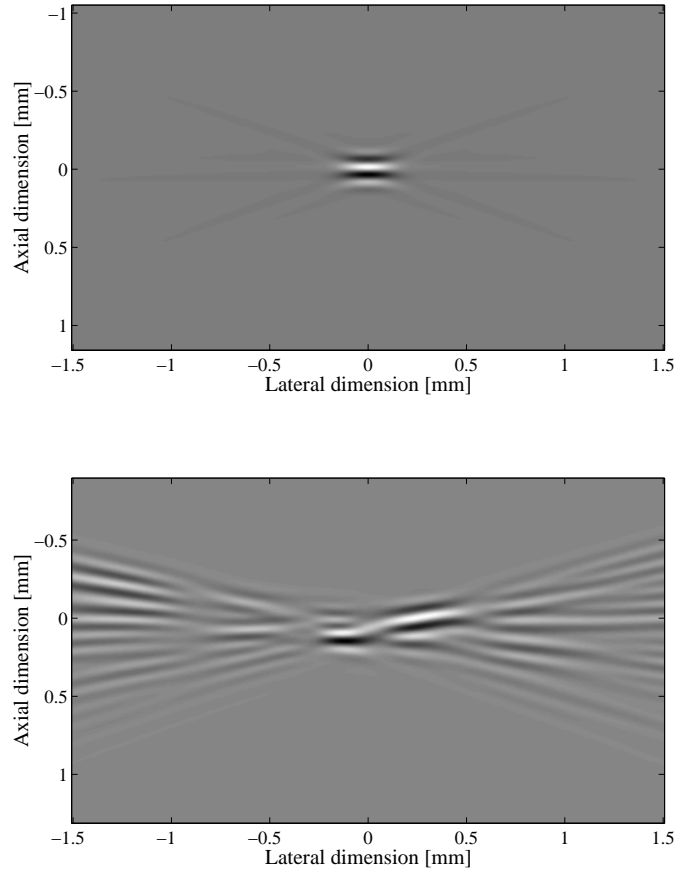
Figure 9.4: The impact of the second order aberrator shown in Fig. 9.2 on the system point spread function. The aberrated case (bottom) is compared to the unaberrated control (top). As in the case of first order aberration, the "sharpness" of the PSF is reduced, reflecting losses of spatial and contrast resolution. Once again, the images are not displayed with the same gray-scale, so they do not show the 91% reduction in PSF amplitude caused by the aberration.

9.4   Detection:

Detection refers to a variety of methods of estimating or approximating the RF echo envelope. Ideally, the detection process shifts the signal band to base band, removing the carrier frequency, as shown in Figure 9.6.

The simplest form of detection is AM demodulation using a full wave rectifier followed by a low pass filter. This is shown schematically in Figure 9.7, using the squaring operation to represent rectification.

A more sophisticated demodulation technique is to mix the signal with that from a local oscillator. This produces base-band and double-frequency components, the latter of which are typically filtered out using a low pass filter. An extension of this concept, known as quadrature demodulation, is to mix the original signal with two local oscillators having the same frequency but shifted by 90° in phase relative to one another. The two baseband signals that remain after low-pass filtering are often referred to as the **I** (for "in-phase") and **Q** (for "quadrature") signals. Generating both I and
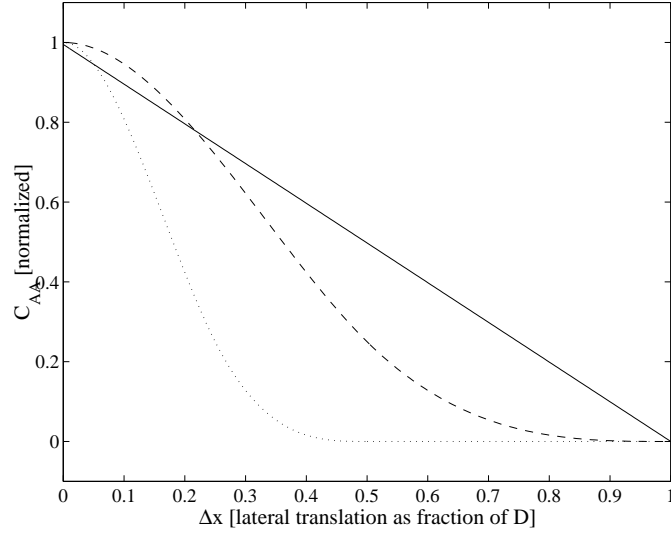
Figure 9.5: The cross-correlation between speckle signals from the focus received on two elements of an array obeys the predictions of the Van Cittert-Zernicke theorem (solid line). Here this curve is compared to the cross-correlation between apertures given lateral translation on receive only (dashed) and on transmit and receive (dotted).

Figure 9.6: Through "ideal" demodulation, the relationships of signal frequency components to the center frequency are translated to the baseband, reestablishing these component relationships relative to DC.

Q signals preserves the phase information in the original signal.

Figure 9.7: If we model rectification with the squaring operation of the echo signal $e(t)$, the frequency domain representation of this detection method is shown above. The original RF signal (left) is convolved with itself to produce base-band and double-frequency components (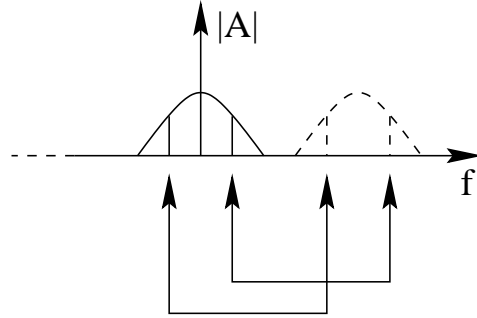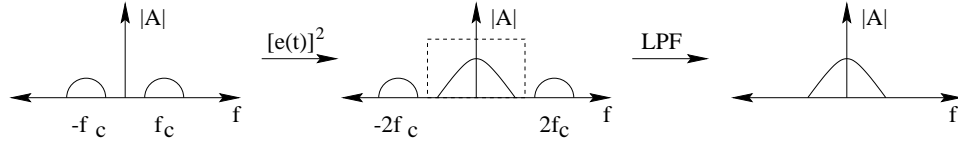center). The application of a low pass filter (LPF) removes the double-frequency components, leaving the desired baseband signal (right).

Given the trigonometric identities,

$$\cos\alpha\sin\beta = \frac{1}{2}[\cos(\alpha - \beta) + \cos(\alpha + \beta)]$$

$$\sin\alpha\sin\beta = \frac{1}{2}[\sin(\alpha + \beta) + \sin(\alpha - \beta)]$$

Consider

$$\alpha = \omega_c$$

$$\text{If } \beta = \omega_c + \Delta\omega_2$$

$$\text{The baseband terms } = \frac{1}{2}\cos(-\Delta\omega_2) = \frac{1}{2}\cos(\Delta\omega_2) \tag{9.1}$$

$$\text{and } = \frac{1}{2}\sin(-\Delta\omega_2) = -\frac{1}{2}\sin(\Delta\omega_2)$$

$$\text{If } \beta = \omega_c - \Delta\omega_1$$

$$\text{The baseband terms } = \frac{1}{2}\cos(\Delta\omega_1)$$

$$\text{and } = -\frac{1}{2}\sin(\Delta\omega_1)$$

Neither of these techniques achieve "ideal" demodulation. While the level of energy at zero Hertz (DC) is preserved, the base-band signal away from DC contains the integration across f of the product of frequencies at shift Δf:

$$\mathbb{F}(\Delta f) = \int_{-BW/2}^{BW/2} f_{axial}(f) f_{axial}(f + \Delta f) df \tag{9.2}$$

The energy at Δf contains the integral of cross products of all frequencies at this shift. The original signal is irreversibly lost. This process mixes spatial frequency components across the bandwidth.

The most accurate demodulation technique is to use the Hilbert operator or the Hilbert transform to generate the quadrature signal at the RF center frequency. This operation does not assume any particular center frequency, and is thus immune to discrepancies between the local oscillator's frequency and that of the echo signal. The echo envelope is then found by calculating the magnitude of the complex signal formed by combining the original RF signal with its synthesized quadrature signal. With this method, no filtering is necessary.

9.5　Elastography imaging

Elastography refers to the imaging of the mechanical elastic properties of tissue[48, 49]. These methods are based on vibrating or compressing the tissue while imaging the tissue with ultrasound. This approach grew from the dynamic palpation of the body during imaging.

Various methods for creating elastic waves or motion in a tissue are under investigation, including an internally or externally applied vibrator, an externally-applied compression paddle, or pumping waves using low frequency sound. Motion under vibration is imaged using Doppler techniques or speckle-tracking techniques. Standing waves are a problem, especially with strong vibration necessary for the targets.

Compression based techniques typically used some kind of correlation search before and after compression. Some error is produced in these techniques by the decorrelation of speckle during compression. Decorrelation during compression results in part from scatterers moving into or out of the resolution volume, and partly from changes in the geometric relationships among particles within the resolution volume[50, 51].

9.6　Limitations of k-space

In closing, it is important to reiterate the various limitations of k-space. The most obvious limitation is that it is a linear systems approach that follows from the Fraunhofer approximation, and thus can only be applied under conditions of linear propagation and within the constraints of that approximation. Thus k-space cannot be applied in analyzing non-linear imaging modalities or the near field. Also, modeling the interaction between an imaging system and scatterers is only straightforward for targets that can be represented as point targets or collections of point targets, and under conditions justifying the Born approximation. There is no obvious means to represent non-Rayleigh scatterers, or to consider conditions in which the Born approximation is unjustified, such as in blood with physiological levels of hematocrit, or a bolus of a microbubble ultrasonic contrast agent. Finally, some k-space operations cannot be applied in the analysis of a spatially shift-variant system, such as in a complex flow field in which shear and turbulence are present that are warping the point-spread function as a function of location.

Despite these limitations, we hope this text has demonstrated the utility of a k-space approach in understanding and analyzing many aspects of ultrasound imaging systems and beamforming techniques.

Bibliography

[1] R. M. Lerner and R. C. Waag. Wave space interpretation of scattered ultrasound. *Ultrasound in Medicine and Biology*, 14(2):97–102, 1988.

[2] W. F. Walker and G. E. Trahey. The application of k-space in medical ultrasound. *IEEE Transactions on Ultrasonics, Ferroelectrics and Frequency Control*, 45:541–558, 1998.

[3] J. A. Jensen and N. B. Svendsen. Calculation of pressure fields from arbitrarily shaped, apodized, and excited ultrasound transducers. *IEEE Transactions on Ultrasonics, Ferroelectrics, and Frequency Control*, 39(2):262–267, 1992.

[4] G. E. Tupholme. Generation of acoustic pulses by baffled plane pistons. *Mathematika*, 16:209–224, 1969.

[5] P. R. Stephanishen. The time-dependent force and radiation impedance on a piston in a rigid infinite planar baffle. *Journal of the Acoustical Society of America*, 49:841–849, 1971.

[6] P. R. Stephanishen. Transient radiation from pistons in a rigid infinite planar baffle. *Journal of the Acoustical Society of America*, 49:1627–1638, 1971.

[7] M. F. Insana and D. G. Brown. Acoustic scattering theory applied to soft biological tissues. In K. K. Shung and G. A. Thieme, editors, *Ultrasonic scattering in biological tissues*, pages 76–124. CRC Press, Boca Raton, 1993.

[8] J. J. Faran. Sound scattering by solid cylinders and spheres. *Journal of the Acoustical Society of America*, 23:405–418, 1951.

[9] A. R. Selfridge. Approximate material properties in isotropic materials. *IEEE Transactions on Sonics and Ultrasonics*, SU-32:381–394, 1985.

[10] S. A. Goss, R. L. Johnston, and F. Dunn. Comprehensive compilation of empirical ultrasonic properties of mammalian tissues. *Journal of the Acoustical Society of America*, 64:423–457, 1978.

[11] S. A. Goss, R. L. Johnston, and F. Dunn. Compilation of empirical properties of mammalian tissues. II. *Journal of the Acoustical Society of America*, 68(1):93–108, 1980.

[12] J. W. Goodman. *Introduction to Fourier Optics*. McGraw-Hill, San Francisco, 1968.

[13] R. N. Bracewell. *The Fourier Transform and Its Applications*. McGraw-Hill, Inc., New York, 1986.

[14] J. A. Campbell and R. C. Waag. Ultrasonic scattering properties of three random media with implications for tissue characterization. *Journal of the Acoustical Society of America*, 75:1879–1886, 1984.

[15] W. J. Davros, J. A. Zagzebski, and E. L. Madsen. Frequency-dependent angular scattering of ultrasound by tissue-mimicking materials and excised tissue. *Journal of the Acoustical Society of America*, 80:229–237, 1986.

[16] M. F. Insana, R. F. Wagner, D. G. Brown, and T. J. Hall. Describing small-scale structure in random media using pulse-echo ultrasound. *Journal of the Acoustical Society of America*, 87:1:179–192, 1990.

[17] M. F. Insana, R. F. Wagner, B. S. Garra, D. G. Brown, and T. H. Shawker. Analysis of ultrasound image texture via generalized rician statistics. *Optical Engineering*, 25(6):743–748, 1986.

[18] M. F. Insana, J. G. Wood, and T. J. Hall. Identifying acoustic scattering sources in normal renal parenchyma in vivo by varying arterial and ureteral pressures. *Ultrasound in Medicine and Biology*, 18:587–599, 1992.

[19] M. F. Insana, T. J. Hall, J. G. Wood, and Z-Y Yan. Renal ultrasound using parametric imaging techniques to detect changes in microstructure and function. *Investigative Radiology*, 28, 8:720–725, 1993.

[20] B. S. Garra, B. H. Krasner, S. C. Horii, Susan Ascher, S. K. Mun, and R. K. Zeman. Improving the distinction between benign and malignant breast lesions: the value of sonographic texture analysis. *Ultrasonic Imaging*, 15:267–285, 1993.

[21] J. G. Miller, J. E. Perez, J. G. Mottley, E. I. Madaras, P. H. Johnston, E. D. Blodgett, L. J. Thommas, III, and B. E. Sobel. Myocardial tissue characterization: an approach based on quantitative backscatter and attenuation. In *Proc. IEEE Ultrasonics Symposium*, pages 782–793, 1983.

[22] J. C. Bamber and C. Daft. Adaptive filtering for reduction of speckle in ultrasonic pulse-echo images. *Ultrasonics*, pages 41–44, 1986.

[23] J.W. Goodman. *Statistical Optics*. Wiley-Interscience, New York, 1985.

[24] J. W. Goodman. Statistical properties of laser speckle patterns. In J.C. Dainty, editor, *Laser Speckle and Related Phenomena*, pages 9–75. Springer-Verlag, Berlin, 1984.

[25] C. B. Burckhardt. Speckle in ultrasound B-mode scans. *IEEE Transactions on Sonics and Ultrasonics*, SU-25(1):1–6, 1978.

[26] R. F. Wagner, M. F. Insana, D. G. Brown, and S. W. Smith. Statistical physics of medical ultrasonic images. *SPIE International Symposium on Pattern Recognition and Acoustical Imaging*, 768:22–27, 1987.

[27] J. M. Thijssen and B. J. Oosterveld. Texture in tissue echograms. *Journal of Ultrasound in Medicine*, 9:215–229, 1990.

[28] R. F. Wagner, M. F. Insana, and S. W. Smith. Fundamental correlation lengths of coherent speckle in medical ultrasonic images. *IEEE Transactions on Ultrasonics, Ferroelectrics and Frequency Control*, 35(1):34–44, 1988.

[29] Gregg E. Trahey and Stephen W. Smith. Properties of acoustical speckle in the presence of phase aberration part I: first order statistics. *Ultrasonic Imaging*, 10:12–28, 1988.

[30] Stephen W. Smith, Gregg E. Trahey, Sylvia M. Hubbard, and Robert F. Wagner. Properties of acoustical speckle in the presence of phase aberration part II: correlation lengths. *Ultrasonic Imaging*, 10:29–51, 1988.

[31] G. E. Trahey, S. W. Smith, and O. T. von Ramm. Speckle pattern correlation with lateral aperture translation: experimental results and implications for spatial compounding. *IEEE Transations on Ultrasonics, Ferroelectrics, and Frequency Control*, UFFC-33(3):257–264, 1986.

[32] Matthew O'Donnell. Optimum displacement for compound image generation in medical ultrasound. *IEEE Transactions on Ultrasonics, Ferroelectrics, and Frequency Control*, 35:470–476, 1988.

[33] H. E. Melton and P. A. Magnin. A-mode speckle reduction with compound frequencies and compound bandwidths. *Ultrasonic Imaging*, 6:159–173, 1984.

[34] G. E. Trahey, J. W. Allison, S. W. Smith, and O. T. von Ramm. A quantitative approach to speckle reduction via frequency compounding. *Ultrasonic Imaging*, 8:151–164, 1986.

[35] M. Moshfeghi and R. C. Waag. In-vivo and in-vitro ultrasound beam distortion measurements of a large aperture and a conventional aperture focused transducer. *Ultrasound in Medicine and Biology*, 14(5):415–428, 1988.

[36] M. O'Donnell and S.W. Flax. Phase aberration measurements in medical ultrasound: human studies. *Ultrasonic Imaging*, 10:1–11, 1988.

[37] Y. Sumino and R. C. Waag. Measurements of ultrasonic pulse arrival time differences produced by abdominal wall specimens. *Journal of the Acoustical Society of America*, 90(6):2924–2930, 1991.

[38] G. E. Trahey, P. D. Freiburger, L. F. Nock, and D. C. Sullivan. In vivo measurements of ultrasonic beam distortion in the breast. *Ultrasonic Imaging*, 13:71–90, 1991.

[39] Qing Zhu and B. D. Steinberg. Large-transducer measurements of wavefront distortion in the female breast. *Ultrasonic Imaging*, 14(3):276–299, 1992.

[40] P. D. Freiburger, D. C. Sullivan, B. H. LeBlanc, S. W. Smith, and G. E. Trahey. Two-dimensional ultrasonic beam distortion in the breast: in vivo measurements and effects. *Ultrasonic Imaging*, 14:398–414, 1992.

[41] Qing Zhu and B. D. Steinberg. Wavefront amplitude distribution in the female breast. *Journal of the Acoustical Society of America*, 96:1–9, 1994.

[42] L. M. Hinkelman, D. L. Liu, L. A. Metlay, and R. C. Waag. Measurements of ultrasonic pulse arrival time and energy level variations produced by propagation through abdominal wall. *Journal of the Acoustical Society of America*, 95(1):530–541, 1994.

[43] L. M. Hinkelman, D-L. Liu, R. C. Waag, Q. Zhu, and B. D. Steinberg. Measurement and correction of ultrasonic pulse distortion produced by the human breast. *Journal of the Acoustical Society of America*, 97(3):1958–1969, 1995.

[44] Qing Zhu, B. D. Steinberg, and R. Arenson. Correlation distance measurements of the female breast. *Journal of the Acoustical Society of America*, 98:694–705, 1995.

[45] M. E. Anderson and G. E. Trahey. The direct estimation of sound speed using pulse-echo ultrasound. *Journal of the Acoustical Society of America*, 104:3099–3106, 1998.

[46] Raoul Mallart and Mathias Fink. The van cittert-zernike theorem in pulse echo measurements. *Journal of the Acoustical Society of America Journal of the Acoustical Society of America*, 90(5):2718–2727, 1991.

[47] S. W. Flax and M. O'Donnell. Phase aberration correction using signals from point reflectors and diffuse scatters: basic principles. *IEEE Transactions on Ultrasonics, Ferroelectrics and Frequency Control*, 35(6):758–767, 1988.

[48] L. Gao, K. J. Parker, R. M. Lerner, and S. F. Levinson. Imaging of the elastic properties of tissue - a review. *Ultrasound in Medicine and Biology*, 22:959–977, 1996.

[49] A. P. Sarvazyan, A. R. Skovaroda, S. Y. Emelianov, J. B. Fowlkes, J. G. Pipe, R. S. Adler, R. B. Buxton, and P. L. Carson. Biophysical bases of elasticity imaging. *Acoustical Imaging*, 21:223–240, 1995.

[50] J. Meunier. Ultrasonic texture motion analysis: theory and simulation. *IEEE Transactions on medical imaging*, 14:293–300, 1995.

[51] M. F. Insana, P. Chaturvedi, T. J. Hall, and M. Bilgen. 3-D companding using linear arrays for improved strain imaging. In *Proceedings of the IEEE Ultrasonics Symposium*, volume 2, pages 1435–1438, 1997.